
Scalar/Contaminant Source Locating in Turbulent Flows

ROWAN L. TAYLOR

Master of Engineering

Supervised by Professor Laurent Mydlarski

Department of Mechanical Engineering
McGill University



McGill

A thesis submitted to McGill University in partial fulfillment of
the requirements for the degree of Master of Engineering

*For my parents, Len and Wendy, who taught me to never stop questioning;
And for Kieran, for her unwavering support and occasional distraction.*

Abstract

The ability to locate the source of a scalar/contaminant emitted in a turbulent flow – using as data the scalar’s concentration measured within the resulting scalar plume and (optionally) the relative velocity of the fluid with respect to the searcher – is relevant to two quite distinct problems: i) the ability of animals to detect the scent of food or mating partners, and ii) the ability of authorities to locate a release (accidental, terrorist, or other) of a noxious (chemical, biological, or radioactive) substance. The majority of the relevant research in this area has been performed by biologists or roboticists, with little input from fluid dynamicists. Given that the vast majority of relevant flows are turbulent, the present work focuses on accurate and efficient scalar/contaminant source locating therein, by attempting to incorporate knowledge of turbulent flows.

To this end, the scalar under consideration is temperature and it is emitted from a line source at the centreline of a fully developed, high-aspect-ratio, turbulent channel flow with a Reynolds number ($Re \equiv \langle U \rangle_{y/h=1} h/\nu$) of 10,800. It is shown that an optimal search algorithm has to balance the trade-offs between explorative and exploitive search phases, since the information available to the searcher is inherently patchy and intermittent. Algorithms which use a root-mean-square (rms)-to-mean ratio ($\theta_{rms}/\Delta T$) of the scalar concentration as the primary search parameter are found to be superior in accuracy, speed, and robustness to noise in a one-dimensional search domain.

It is furthermore shown that the maximum benefit of incorporating the physics of turbulent flows is achieved in a two- (or three-) dimensional search domain, and preliminary results indicate that an infotactic search algorithm using a five-parameter plume model for either the mean scalar concentration (ΔT) or rms fluctuation (θ_{rms}) is expeditious and accurate.

Résumé

La localisation de l'origine d'un contaminant/scalaire émis dans un écoulement turbulent – en utilisant la concentration mesurée du scalaire dans le panache et (facultativement) la vitesse du fluide relative au chercheur – se rapporte à deux problèmes distincts : i) la capacité des animaux à détecter le parfum de la nourriture ou des partenaires sexuels, et ii) la capacité des autorités à localiser un dégagement (accidentel, terroriste ou autre) d'une substance nocive (chimique, biologique ou radioactive). La majorité des travaux de recherche pertinents a été réalisée par des biologistes ou les roboticiens, avec peu d'apport des mécaniciens des fluides. Étant donné que la grande majorité des écoulements concernés sont turbulents, le présent travail se concentre sur la localisation précis et efficace de l'origine d'un scalaire, en intégrant les connaissances des écoulements turbulents.

À cette fin, un scalaire (la température) est émis par une source linéaire au centre d'un écoulement en canal, pleinement développé, de grand rapport hauteur/largeur et avec un nombre de Reynolds ($Re \equiv \langle U \rangle_{y/h=1} h/\nu$) de 10.800. Il est démontré que l'algorithme de recherche optimal doit atteindre un juste équilibre entre les phases de recherche exploratoires et exploiteuses, puisque les données à la disposition du chercheur sont intrinsèquement inégales et intermittentes. L'utilisation d'un rapport de l'écart type à la moyenne ($\theta_{rms}/\Delta T$) de la concentration du scalaire comme paramètre de recherche primaire donne des algorithmes de recherche supérieurs en termes de précision, vitesse et insensibilité au bruit en domaine de recherche unidimensionnel.

L'avantage maximal de l'intégration de la physique des écoulements turbulents est réalisé dans un domaine de recherche à deux (ou trois) dimensions, et les résultats préliminaires indiquent qu'un algorithme de recherche infotactique à l'aide d'un modèle de panache à cinq paramètres (pour soit la concentration moyenne scalaire (ΔT) ou l'écart type (θ_{rms})) est rapide et précis.

Acknowledgements

I would like to extend my sincere gratitude to all those who have helped me and supported me in this work. First and foremost, I would like to thank my supervisor, Professor Laurent Mydlarski, as this work would not have been possible without his input as my supervisor, teacher, and friend.

I would also like to thank the members of the turbulence team, both past and present: Jason Lepore, with whom I worked side by side for most of my time at McGill, for his guidance and help; Emmanuel Germaine, for his careful assistance with aligning the channel and comparing initial results; Samer Afara and James Mevdeseck, for their help with parts of the experimental setup; and also Arpi Berajeklian, for her help in smoothing my arrival at McGill.

My thanks are also extended to Mario Iacobaccio for assistance with difficult-to-find hardware; Professor Bantwall Baliga for his excellent courses and any-time-of-day advice; Nosa Mohammed for IT support; past and present graduate administrators Joyce Nault, Antonella Fratino and Shirley Baxendale; and all other McGill support staff with whom I have dealt.

I am thankful for the many influential teachers and colleagues at Carleton University who helped found my engineering education, and for all those at Thomson House who kept me fed and watered during my studies.

I am also extremely grateful for the support of my friends and family, here in Montreal and elsewhere, who supported and kept me sane through this endeavour.

Lastly, I would like to extend my sincere appreciation and gratitude to the National Science and Engineering Council of Canada (NSERC) for funding my research through grants to my supervisor.

Contents

1	Background and Motivation	1
1.1	Introduction	1
1.2	Background Theory	4
1.2.1	Reynolds-Averaged Governing Equations	5
1.2.2	Turbulent Kinetic Energy Budget	6
1.2.3	Passive Scalar Variance Budget	7
1.2.4	Wall-Bounded Shear Flow	8
1.3	Literature Review	10
1.3.1	Scalar Mixing	11
1.3.1.1	Diffusion	11
1.3.1.2	Advection	11
1.3.1.3	Turbulent Transport	12
1.3.2	Source Locating	13
1.3.2.1	Search Phases	15
1.3.2.2	Kinesis-based Algorithms	16
1.3.2.3	Surge-Based Algorithms	18
1.3.2.4	Single Searcher Taxis-Based Algorithms	22
1.3.2.5	Swarm Taxis-Based Algorithms	25
1.4	Thesis Objectives and Overview	27
1.4.1	Thesis Objectives	27
1.4.2	Thesis Overview	28
2	Experimental Setup	29
2.1	The Wind Tunnel	30
2.1.1	Coordinate System	33
2.1.2	Scalar Source	33
2.1.3	Traversing Mechanism	35

2.2	Measurement Techniques	35
2.2.1	Probe Setup	37
2.2.2	Hot-Wire Anemometry	37
2.2.2.1	Hot-Wire Calibration	39
2.2.3	Cold-Wire Thermometry	39
2.2.3.1	Cold-Wire Calibration	41
2.2.4	Mean Ambient Temperature Measurement	42
2.2.5	Spatial and Temporal Resolution	43
2.2.5.1	Spatial Resolution	43
2.2.5.2	Temporal Resolution	44
2.3	Data Acquisition	45
2.3.1	Hot-Wire Measurements	45
2.3.2	Cold-Wire Measurements	46
2.3.3	Analogue to Digital Conversion	46
3	Flow Validation and Experimental Conditions	47
3.1	Flow Validation	47
3.1.1	Fully Developed, One-Dimensional Channel Flow	48
3.1.1.1	Physical Integrity of the Channel	48
3.1.1.2	Velocity Field	49
3.1.2	Passivity of the Scalar Field	53
3.1.3	Source Obstruction Effects	54
3.1.4	z-direction Invariance	54
3.1.5	Adiabatic Channel Walls	54
3.2	Experimental Conditions	55
4	Results and Discussion	60
4.1	The Scalar Field	61
4.1.1	Sources of Error	63
4.1.1.1	Positioning Error	63
4.1.1.2	Cold-Wire Probe Differences	64
4.1.1.3	Reduced Statistical Convergence in the Edges of the Plume	64
4.1.1.4	Other Sources of Error	64
4.1.2	Downstream Evolution	65
4.2	Algorithm Development	67
4.2.1	Search Parameters	67

4.2.2	Convergence Analysis	68
4.2.3	Starting Position	70
4.2.4	Binary Plume Threshold	70
4.2.5	Plume Finding/Explorative Phase	72
4.2.6	Plume Traversal/Exploitive Phase	72
4.2.7	Algorithm Template	73
4.3	One-Dimensional Search Domain Results	74
4.4	Two-Dimensional Search Domain Results	80
4.4.1	Scalar Field Model	81
4.4.2	Sample Search	83
4.4.3	Source Declaration	86
4.4.4	Detailed Results	86
5	Conclusions and Future Work	89
5.1	Conclusions	89
5.2	Future Work	91
	Bibliography	93

List of Figures

1.1	Hierarchal view of search strategies	15
1.2	Division of search phases	16
1.3	Sketch of basic kinesis and taxis search strategies	17
1.4	Sketch of the casting algorithm	18
1.5	Sketch of the surge-spiral algorithm	19
1.6	Sketch of the surge-cast algorithm	20
1.7	The Balkovsky search cones	21
1.8	Sketch of a simple moth strategy trajectory	22
1.9	Search trajectories for causality- and high likelihood-cones	23
1.10	Typical search trajectories for the infotaxis strategy	24
2.1	High-aspect-ratio channel	29
2.2	Channel port locations	32
2.3	Test section schematic	34
2.4	Experiment top view	35
2.5	2D traversing mechanism setup	36
2.6	2D traversing mechanism schematic	36
2.7	TSI probe parts	38
2.8	Laminar calibration jet	40
2.9	Laminar calibration jet schematic	40
2.10	Hot-wire calibration curve	41
2.11	Cold-wire calibration curve	42
2.12	Cold-wire time constant curve	45
3.1	Channel curvature measuring setup	49
3.2	Mean longitudinal velocity profiles	51
3.3	RMS longitudinal velocity fluctuation profiles	52
3.4	Near-wall longitudinal mean velocity profile	53

3.5	Skewness and kurtosis of longitudinal velocity fluctuations	56
3.6	Non-dimensionalized spectra	58
4.1	Sample temperature fluctuation statistics profiles	62
4.2	Comparison of the downstream evolution of the scalar field	66
4.3	Statistical convergence at the centreline	69
4.4	Convergence of the scalar statistics	71
4.5	Mean temperature excess search results	77
4.6	RMS temperature fluctuation search results	78
4.7	RMS-to-mean ratio search results	78
4.8	RMS-to-mean ratio search results	79
4.9	Comparison of search parameter accuracies	80
4.10	2D mean temperature excess profile	84
4.11	Sample search fit evolution	85

List of Tables

3.1	Channel width measurements	48
3.2	Channel curvature measurements	49
3.3	Summary of flow properties	59
4.1	Cold-wire probe frequency response	64
4.2	1D search results for select parameters	77
4.3	Summary of 2D search results for peak mean temperature difference	88
4.4	Summary of 2D search results for rms temperature fluctuation	88

Nomenclature

Roman

A	hot-wire calibration constant (offset), or plume model constant
B	hot-wire calibration constant (slope), or plume model constant
C	constant (for a coordinate in the plume model)
$D(\kappa)$	dissipation spectrum
De	Dean number
d_s	thermal line source diameter
E	electrical potential (voltage)
$E(\kappa)$	three-dimensional energy spectrum
$E_{11}(\kappa_1)$	one-dimensional longitudinal spectrum
f	frequency
f_c	cut-off frequency
g	gravity vector
h	channel half-width
K_u	Kurtosis of longitudinal velocity fluctuations
K_θ	Kurtosis of temperature (scalar) fluctuations
L	length
ℓ	integral length scale of the velocity field
ℓ_θ	integral length scale of the thermal field
m	hot-wire calibration constant, or plume model exponent
n	hot-wire calibration constant exponent, or plume model exponent
\tilde{P}	instantaneous modified pressure
$\langle P \rangle$	average modified pressure
Pe	Peclet number
Pr	Prandtl number
R	line-fit correlation coefficient

R_c	radius of curvature
Re	Reynolds number
Re_*	friction Reynolds number
Re_s	thermal source Reynolds number
R_ℓ	Reynolds number based on the integral length scale
R_λ	Taylor-scale Reynolds number
R_τ	turbulent Reynolds number
S_u	Skewness of longitudinal velocity fluctuations
S_θ	Skewness of temperature (scalar) fluctuations
$\langle S_{ij} \rangle$	mean fluctuating strain rate
$\langle s_{ij} \rangle$	fluctuating strain rate
T_{film}	film temperature
T_∞	free-stream temperature
T_s	thermal line source temperature
$\langle T \rangle$	mean temperature
$\widetilde{\Delta T}$	instantaneous temperature excess
$\langle \Delta T \rangle$	mean temperature excess
ΔT_{peak}	peak mean temperature excess
t_L	integral time scale (at the channel centreline)
t	time
t_s	total sampling time
U	velocity
U_c	centreline velocity
U_∞	freestream velocity
\tilde{U}_i	instantaneous velocity
$\langle U_i \rangle$	average velocity
u_i	velocity fluctuation
u_{rms}	root-mean-square velocity fluctuation
u^+	non-dimensionalized velocity
u_*	friction velocity
w	half-width of the thermal plume
y^+	non-dimensionalized wall-normal coordinate
y_s	true wall-normal line source position
y'_s	measured/calculated/predicted/declared wall-normal line source position
x, y, z	Cartesian coordinates

Greek

α	thermal diffusivity
δ_ν	viscous length scale
ϵ	dissipation rate of turbulent kinetic energy (TKE)
ϵ_θ	dissipation rate of scalar variance $\langle \theta^2 \rangle$
η	Kolmogorov microscale of length (velocity field)
η_θ	Kolmogorov microscale of length (scalar field)
Γ	scalar diffusivity
γ	molecular diffusivity
Θ	scalar
$\tilde{\Theta}$	instantaneous scalar
$\langle \Theta \rangle$	average scalar
θ	temperature (scalar) fluctuation
θ_{rms}	rms of the temperature fluctuation
$\theta_{rms-peak}$	peak rms temperature fluctuation
κ	three-dimensional wavenumber, or von Kàrmàn constant
κ_1	longitudinal wavenumber
λ	Taylor microscale of length
ν	kinematic fluid viscosity
ν_T	turbulent viscosity
ρ	fluid density
σ	Gaussian standard deviation
σ_{b-n}	background noise level
σ_{mean}	standard deviation of the mean temperature excess profile
σ_{rms}	standard deviation of the rms temperature fluctuation profile
σ_{ys}	standard deviation of the declared line source position profile
\mathcal{S}_{param}	standard deviation of distribution of quantity <i>param</i>
τ_ℓ	integral time scale
τ_η	Kolmogorov microscale of time
τ_{cw}	cold-wire time constant
τ_w	wall shear stress

Abbreviations

1D	one-dimensional
2D	two-dimensional
3D	three-dimensional
b	(number of) data block(s)
BNC	Bayonet Neill-Concelman (connector)
CCA	constant current anemometer
CL	centreline
CTA	constant temperature anemometer
CV	control volume
CWT	cold-wire thermometry
DAQ	data acquisition
FWHM	full-width at half-maximum
HWA	hot-wire anemometry
K41	Kolmogorov (1941) theory
KOC	Kolmogorov-Obukhov-Corrsin theory
NS	Navier-Stokes equations
PDF	probability density function
RANS	Reynolds-averaged Navier-Stokes equations
rms	root-mean-square
rpm	revolutions per minute
spb	(number of) samples per data block
VI	virtual instrument (in LabVIEW)

This page intentionally left blank.

Chapter 1

Background and Motivation

1.1 Introduction

*In nature's infinite book of secrecy
A little I can read.*¹

Fluid mechanics is a fundamental underpinning of engineering. Its formal study is thought to have originated in ancient Greece with the work of Archimedes on fluid statics and buoyancy. Advances in the field continued through the ages with the work of Pascal, Newton, Bernoulli, and Euler, amongst others, during the seventeenth and eighteenth centuries.

The significant attention paid to fluid mechanics is related to the realization that it plays an important role in an enormous range of engineering applications. Fluid mechanics is relevant to many systems, both biological (e.g., the cardiovascular circulation system) and engineered (e.g., electricity generation from coal- and nuclear-powered steam turbines, as well as from hydro- and wind-powered turbines). Furthermore, all forms of transportation (e.g., aircraft, boats, and cars) as well as many

1. Shakespeare, *Antony and Cleopatra*. Act I, Scene II.

energy distribution systems (e.g., oil and natural gas pipelines) require an understanding of fluid mechanics.

Fluid flows are classically divided into three types: i) laminar, ii) transitional, and iii) turbulent. The latter is by far the most prevalent, in both natural (e.g., the atmospheric boundary layer) and man-made (e.g., oil pipeline) flows. Although the first early descriptions of turbulent flows can be credited to Leonardo da Vinci, it was Osbourne Reynolds who performed the first rigorous classification experiments in the late nineteenth century.

While aboard a whaling ship taking part in a meteorological study off the east coast of Canada in the early twentieth century, Sir G.I. Taylor became interested in the mixing of contaminants in turbulent flows (as seen in the steamer's exhaust), and, a few years after his return, he published a study of turbulence describing this phenomenon. Soon after, in the early nineteen-twenties, L.F. Richardson first wrote of the turbulent cascade, described in the following short poem:

*Big whirls have little whirls,
which feed on their velocity.
Little whirls have lesser whirls,
and so on to viscosity
(in the molecular sense).²*

Richardson was describing how motions over the large range of scales present in a turbulent flow are all related through the energy cascade. If a turbulent flow is considered to be composed of different-sized eddies, each with its own characteristic size, velocity, and timescale, then the largest eddies must have a size comparable to the large-scale geometry of the flow. However, the larger eddies are unstable and break up, successively transferring their kinetic energy into smaller and smaller eddies until the kinetic energy is finally converted into internal energy by the action of viscosity. This process is referred to as the turbulent energy cascade.

2. Richardson, L.F. 1925. *Big Whirls*.

The pioneering work of Kolmogorov (1941) extended Richardson's ideas and postulated the concept of local isotropy, which is arguably the most important scientific contribution to the study of turbulence. The postulate of local isotropy states that, at high Reynolds numbers, the behaviour (i.e., velocity field) of the smallest scales in turbulent flows should be universal. This is in contrast to the large-scale eddies which are generally anisotropic and determined primarily by the different boundary conditions (e.g., flow geometry).

What Taylor saw mixing in the steamer's exhaust was not the fluid itself, but rather small particulates. This is an example of a passive scalar, defined as "a diffusive contaminant in a fluid flow that is present in such a low concentration that it has no dynamical effect (such as buoyancy) on the fluid motion itself" (Warhaft, 2000). Other examples of scalars can include small temperature excesses, chemical species, and biological cues. The mixing of scalars within a fluid flow is of immediate relevance to many processes, both natural and man-made. Examples include pollutant dispersion in the atmosphere and mixing of reactants in combustors.

One of the most useful characteristics of turbulence is its ability to mix fluids and any species (e.g., scalars) contained therein much more effectively than a laminar flow. Consequently, a considerable body of work exists for understanding and predicting the results of the mixing process. Kolmogorov's early work describing the energy cascade and local isotropy of the velocity field was extended to the scalar field by Obukhov (1949) and Corrsin (1951) (together known as KOC theory), and resulted in a greatly improved understanding of the nature of scalar turbulence.

While the enhanced mixing ability that turbulence provides is useful in many applications, it also makes certain problems more difficult. Since a scalar contained in turbulent flow will be mixed much more readily than if it were contained in a laminar flow, the problem of locating the original source of such a species is more challenging.

The ability to accurately and efficiently locate a scalar source in a turbulent flow is the subject of the present work.

1.2 Background Theory

The governing equations of fluid motion for a Newtonian, constant-property fluid are shown below and are equally applicable to laminar, transitional, and turbulent flows. Using tildes to indicate instantaneous quantities, the continuity and momentum Navier-Stokes (NS) equations, written in Cartesian coordinates are, respectively:

$$\frac{\partial \tilde{U}_i}{\partial x_i} = 0, \text{ and} \quad (1.1)$$

$$\frac{\partial \tilde{U}_i}{\partial t} + \tilde{U}_j \frac{\partial \tilde{U}_i}{\partial x_j} = -\frac{1}{\rho} \frac{\partial \tilde{P}}{\partial x_i} + \nu \frac{\partial^2 \tilde{U}_i}{\partial x_j \partial x_j} . \quad (1.2)$$

The instantaneous advection-diffusion equation for a conserved scalar in the flow is:

$$\frac{\partial \tilde{\Theta}}{\partial t} + \tilde{U}_j \frac{\partial \tilde{\Theta}}{\partial x_j} = \Gamma \frac{\partial^2 \tilde{\Theta}}{\partial x_j \partial x_j} . \quad (1.3)$$

Here \tilde{U}_i is the instantaneous velocity vector, \tilde{P} is the instantaneous modified pressure (including the effects of gravity), and $\tilde{\Theta}$ is the instantaneous scalar – e.g., a small temperature excess, or chemical species concentration. ρ is the (constant, and therefore uniform) fluid density, ν is the kinematic viscosity of the fluid, and Γ is the scalar’s molecular diffusivity. In the case of a temperature excess, it is the scalar’s thermal diffusivity (α), whereas in the case of chemical concentration, it is the molecular diffusivity (γ).

Analytical solutions to the governing equations can be found for certain laminar

flows. However, since the equations are three-dimensional, chaotic, time-dependent, and extremely sensitive to initial and boundary conditions, analytical solutions are not known to exist in the turbulent case. To make the problem more tractable, equations for the mean and fluctuating quantities can be derived.

1.2.1 Reynolds-Averaged Governing Equations

In turbulent flows, the instantaneous velocity components (and therefore scalar field) vary randomly in both space and time. Dividing each instantaneous velocity component, \tilde{U}_i , into a sum of its mean, $\langle U_i \rangle$, and a (turbulent) fluctuation, u_i , yields $\tilde{U}_i = \langle U_i \rangle + u_i$. Similarly, for the scalar field, $\tilde{\Theta} = \langle \Theta \rangle + \theta$. This is known as the Reynolds decomposition. Applying this decomposition to the instantaneous governing equations and then averaging them results in Reynolds-averaged equations for the hydrodynamic and scalar fields.

The mean continuity equation becomes simply $\frac{\partial \langle U_i \rangle}{\partial x_i} = 0$. After some manipulation and simplification, the Reynolds-Averaged Navier-Stokes (RANS) equations reduce to:

$$\frac{\partial \langle U_i \rangle}{\partial t} + \langle U_j \rangle \frac{\partial \langle U_i \rangle}{\partial x_j} = -\frac{1}{\rho} \frac{\partial \langle P \rangle}{\partial x_i} + \frac{\partial}{\partial x_j} \left(\nu \frac{\partial \langle U_i \rangle}{\partial x_j} - \langle u_i u_j \rangle \right). \quad (1.4)$$

The new term, $\langle u_i u_j \rangle$, is called the Reynolds stress. It arises from the nonlinear terms and poses a closure problem to this equation.

A similar manipulation can be performed on the advection-diffusion equation for a passive scalar, yielding:

$$\frac{\partial \langle \Theta \rangle}{\partial t} + \langle U_j \rangle \frac{\partial \langle \Theta \rangle}{\partial x_j} = \frac{\partial}{\partial x_j} \left(\Gamma \frac{\partial \langle \Theta \rangle}{\partial x_j} - \langle \theta u_j \rangle \right). \quad (1.5)$$

The new turbulent scalar flux term, $\langle \theta u_j \rangle$, is generated by the nonlinear terms and

again poses a closure problem.

1.2.2 Turbulent Kinetic Energy Budget

Since the kinetic energy of the flow is of interest in the study of turbulence, it is useful to derive a turbulent kinetic energy (TKE) budget. The evolution of the turbulent velocity fluctuations is described in terms of their variance, $\langle u_i u_i \rangle$. The turbulent kinetic energy (TKE) ($= \frac{1}{2} \langle u_i u_i \rangle$) budget can be derived by multiplying the NS equations by the instantaneous velocity, Reynolds-averaging, and then subtracting the mean kinetic energy to yield:

$$\begin{aligned} \frac{\bar{D}}{\bar{D}t} \left(\frac{1}{2} \langle u_i u_i \rangle \right) &= \overbrace{\frac{\partial}{\partial t} \left(\frac{1}{2} \langle u_i u_i \rangle \right)}^a + \overbrace{\langle U_j \rangle \frac{\partial}{\partial x_j} \left(\frac{1}{2} \langle u_i u_i \rangle \right)}^b = \\ &= - \frac{\partial}{\partial x_j} \left[\overbrace{\frac{1}{\rho} \langle u_j p \rangle}^c + \overbrace{\frac{1}{2} \langle u_i u_i u_j \rangle}^d - \overbrace{2\nu \langle u_i s_{ij} \rangle}^e \right] - \overbrace{\langle u_i u_j \rangle \langle S_{ij} \rangle}^f - \overbrace{2\nu \langle s_{ij} s_{ij} \rangle}^g . \end{aligned} \quad (1.6)$$

Noting that $\langle S_{ij} \rangle = \frac{1}{2} \left(\frac{\partial \langle U_i \rangle}{\partial x_j} + \frac{\partial \langle U_j \rangle}{\partial x_i} \right)$ is the mean fluctuating rate of strain, and $s_{ij} = \frac{1}{2} \left(\frac{\partial u_i}{\partial x_j} + \frac{\partial u_j}{\partial x_i} \right)$ is the fluctuating rate of strain, the above terms have the following physical interpretations:

- a) $\frac{\partial}{\partial t} \left(\frac{1}{2} \langle u_i u_i \rangle \right)$ is the time rate of change of TKE at a fixed point
- b) $\langle U_j \rangle \frac{\partial}{\partial x_j} \left(\frac{1}{2} \langle u_i u_i \rangle \right)$ is the advection of TKE by the mean flow
- c) $-\frac{\partial}{\partial x_j} \left[\frac{1}{\rho} \langle u_j p \rangle \right]$ is the pressure transport/work done by pressure fluctuations
- d) $-\frac{\partial}{\partial x_j} \left[\frac{1}{2} \langle u_i u_i u_j \rangle \right]$ is the advection of TKE by the fluctuating velocities
- e) $\frac{\partial}{\partial x_j} [2\nu \langle u_i s_{ij} \rangle]$ is the molecular diffusion of TKE by viscosity
- f) $-\langle u_i u_j \rangle \langle S_{ij} \rangle$ is the production of TKE – an exchange of energy between the main flow and the turbulence

g) $-2\nu \langle s_{ij}s_{ij} \rangle$ is the dissipation of TKE (into internal energy) by viscosity

1.2.3 Passive Scalar Variance Budget

Using an analogous approach, an equation for the passive scalar variance budget can be found, noting that $\frac{1}{2} \langle \theta^2 \rangle$ is (one half of) the scalar variance, and not an absolute measure of the scalar itself:

$$\begin{aligned} \frac{\bar{D}}{\bar{D}t} \left(\frac{1}{2} \langle \theta^2 \rangle \right) &= \overbrace{\frac{\partial}{\partial t} \left(\frac{1}{2} \langle \theta^2 \rangle \right)}^a + \overbrace{\langle U_j \rangle \frac{\partial}{\partial x_j} \left(\frac{1}{2} \langle \theta^2 \rangle \right)}^b = \\ &+ \frac{\partial}{\partial x_j} \left[\overbrace{\frac{1}{2} \langle \theta^2 u_j \rangle}^c - \overbrace{\Gamma \frac{\partial}{\partial x_j} \left(\frac{1}{2} \langle \theta^2 \rangle \right)}^d \right] - \overbrace{\langle \theta u_j \rangle \frac{\partial \langle \theta \rangle}{\partial x_j}}^e - \overbrace{\Gamma \left\langle \frac{\partial \theta}{\partial x_j} \frac{\partial \theta}{\partial x_j} \right\rangle}^f. \end{aligned} \quad (1.7)$$

The terms can be interpreted as follows:

- a) $\frac{\partial}{\partial t} \left(\frac{1}{2} \langle \theta^2 \rangle \right)$ is the time rate of change of $\frac{1}{2} \langle \theta^2 \rangle$ at a fixed point
- b) $\langle U_j \rangle \frac{\partial}{\partial x_j} \left(\frac{1}{2} \langle \theta^2 \rangle \right)$ is the advection of $\frac{1}{2} \langle \theta^2 \rangle$ by the mean flow
- c) $\frac{\partial}{\partial x_j} \left[\frac{1}{2} \langle \theta^2 u_j \rangle \right]$ is the advection of $\frac{1}{2} \langle \theta^2 \rangle$ by the turbulent velocity fluctuations
- d) $-\frac{\partial}{\partial x_j} \left[\Gamma \frac{\partial}{\partial x_j} \left(\frac{1}{2} \langle \theta^2 \rangle \right) \right]$ is the diffusion of $\frac{1}{2} \langle \theta^2 \rangle$ by molecular processes
- e) $-\langle \theta u_j \rangle \frac{\partial \langle \theta \rangle}{\partial x_j}$ is the production of $\frac{1}{2} \langle \theta^2 \rangle$
- f) $-\Gamma \left\langle \frac{\partial \theta}{\partial x_j} \frac{\partial \theta}{\partial x_j} \right\rangle = \epsilon_\theta$ is the (molecular) dissipation/smearing of $\frac{1}{2} \langle \theta^2 \rangle$

Now that the governing equations have been presented, it is useful to consider the simplifications that can be made in the case of a wall-bounded turbulent shear flow.

1.2.4 Wall-Bounded Shear Flow

The present work was conducted in a high-aspect-ratio, fully developed and turbulent channel flow (see Chapters 2 and 3). In this particular case of wall-bounded turbulent flows, the governing mean streamwise (x -direction) and cross-stream (y -direction) momentum equations reduce to:

$$0 = -\frac{1}{\rho} \frac{\partial \langle P \rangle}{\partial x} - \frac{\partial \langle uv \rangle}{\partial y} + \nu \frac{\partial^2 \langle U \rangle}{\partial^2 y}, \text{ and} \quad (1.8)$$

$$0 = -\frac{1}{\rho} \frac{\partial \langle P \rangle}{\partial y} - \frac{\partial \langle v^2 \rangle}{\partial y}. \quad (1.9)$$

Consideration of the force balance on an infinitesimal control volume (CV) of length δx in the streamwise direction yields:

$$\begin{aligned} \Sigma F_x = 0 &= P(2hL) - \left(P + \frac{dP}{dx} \delta x \right) (2hL) - 2 \times L\tau_w \delta x \\ \Rightarrow \tau_w &= -h \frac{dP}{dx}, \end{aligned} \quad (1.10)$$

where h is the channel half-width, L is the channel height, and τ_w is the wall shear stress. With τ_w known, selection of suitable characteristic viscous scales for a two-dimensional, statistically steady, fully developed channel flow with with characteristic (geometrical) integral length scale h yields:

$$u_* = u_\tau = \sqrt{\frac{\tau_w}{\rho}} = \text{friction velocity}, \quad (1.11)$$

$$\delta_\nu = \frac{\nu}{u_*} = \text{viscous length scale, and} \quad (1.12)$$

$$Re_* = Re_\tau = \frac{u_* h}{\delta_\nu} = \text{friction Reynolds number}. \quad (1.13)$$

The wall-normal coordinate and mean velocity can thus be non-dimensionalized as:

$$y^+ = \frac{y}{\delta_\nu} = \frac{yu_*}{\nu}, \text{ and} \quad (1.14)$$

$$u^+ = \frac{\langle U \rangle}{u_*}. \quad (1.15)$$

Far from the wall, the wall-normal coordinate is non-dimensionalized instead as $\eta = y/h$. The flow is typically divided into four regions:

The viscous sublayer is defined for $y^+ < 5$ and marks the region of the flow where viscosity is dominant. The viscous stresses are much larger than the Reynolds stresses in this region.

The buffer layer is located from $5 < y^+ < 30$, and separates the viscous and inertial sublayers. Peak production of TKE occurs in this region.

The inertial sublayer or sometimes *log-law layer* falls within the range of wall-normal coordinates where $y^+ > 30$ and $\eta < 0.3$. The log-law designation refers to the fact that when plotted non-dimensionally, a logarithmic mean velocity profile results.

The core region is found where $0.3 < \eta < 1$, i.e., where the mean velocity profile is dictated by its geometry. This region extends to the channel centreline.

It should be noted that the presence of a distinct inertial sublayer requires a high enough Re to sufficiently separate the scales so that the simultaneous conditions $y/(\nu/u_*) \gg 1$ and $y/h \ll 1$ are satisfied. If these conditions are met, asymptotic matching of the solutions to the non-dimensionalized Reynolds-averaged Navier-Stokes equations (1.8 and 1.9) in the limits $y^+ \rightarrow \infty$, $\eta \rightarrow 0$ yields:

$$u^+ = \frac{1}{\kappa} \ln(y^+) + A. \quad (1.16)$$

Here $\kappa \approx 0.41 \pm 5\%$ (the von Kàrmàn constant) and $A \approx 5.2 \pm 5\%$ (Pope, 2000).

The logarithmic velocity profile described by Equation 1.16 is of course only valid for $\eta \ll 1$ and $y^+ \gg 1$. It can also be shown that in the viscous sublayer ($y^+ < 5$), $u^+ = y^+$.

With a basic theoretical understanding of the nature of turbulent channel flow, it is now possible to consider the problem of source locating within such a flow.

1.3 Literature Review

Source locating is relevant to two quite distinct problems: i) the ability of animals to detect food or (the scent of) mating partners, and ii) the ability of authorities to locate a release (accidental, terrorist, or other) of a noxious (chemical, biological, or radioactive) substance. It is a problem predominantly studied in two fields: i) biology, and ii) robotics. The body of work in both fields has grown large in recent years, and, as such, this literature review can only be partial. Works and results most useful for the current project are briefly summarized herein.

While biologists often focus on documenting animals' olfactory search methods for the source of chemical cues (e.g., the scent of food, sex pheromones), roboticists tend to focus on the design of sensors and algorithms for (chemical, biological, or radioactive) contaminant source locating. Both groups have sought guidance from fluid dynamicists on how to better characterize and understand the fluid flows in their applications.

The goal of the present review is to show where a rigorous knowledge of the fundamental fluid mechanics of turbulent flows will be beneficial to existing work. This will aid in creating and optimizing scalar/contaminant source locating algorithms, to increase the accuracy and efficiency of locating a scalar source emitted in a turbulent flow.

1.3.1 Scalar Mixing

As previously discussed, the mixing of scalars within a fluid flow is of immediate relevance to many processes, both natural and man-made. Turbulent mixing is of particular interest for the present work, and it consists of two primary modes of mixing: diffusion and advection.

1.3.1.1 Diffusion

In an effectively stationary fluid environment (very low Reynolds and Peclet numbers, i.e., Re and $Pe \ll 1$), scalars are mixed only by diffusion. This is primarily relevant to chemical transport at the cellular level (Webster & Weissburg, 2009). The scalar, Θ , can represent many physical properties, though in the context of this review it typically denotes either the concentration of a chemical species or a small temperature excess. In such a case, the scalar's transport can be described by the equation for Fickian diffusion:

$$\frac{\partial \tilde{\Theta}}{\partial t} = \Gamma \frac{\partial^2 \tilde{\Theta}}{\partial x_i \partial x_i}, \quad (1.17)$$

where Γ is the (constant and uniform) diffusivity of the scalar. As mentioned, this type of transport is primarily relevant to cellular processes; in fact, in a water-like environment, motion of a cell of less than 20 μm has almost no effect on the chemical flux because the diffusive timescales are smaller than the advective ones (Webster & Weissburg, 2009).

1.3.1.2 Advection

Compared with the purely diffusive case, an overall fluid motion relative to the searcher adds an advective flux of the scalar to the governing equations. The advection-

diffusion equation describes the net transport:

$$\frac{\partial \tilde{\Theta}}{\partial t} + U_i \frac{\partial \tilde{\Theta}}{\partial x_i} = \Gamma \frac{\partial^2 \tilde{\Theta}}{\partial x_i \partial x_i} . \quad (1.18)$$

At low enough Re , the flow remains laminar. This type of flow is usually only applicable to very small organisms, as well as the flow around chemosensory appendages of larger organisms (Webster & Weissburg, 2009). However, source locating in laminar flow has received some study, notably in the robotics field by Lochmatter *et al.* (2008, 2009) and Lochmatter & Martinoli (2009).

1.3.1.3 Turbulent Transport

Of particular interest in the present work is source locating in flows with supercritical (large) Re , i.e., flows that are turbulent. Additional scalar mixing is created by advective transport due to velocity fluctuations in the flow. “A First Course in Turbulence” by Tennekes & Lumley (1972) and “Turbulent Flows” by Pope (2000) are two classic references on the subject of turbulence. Warhaft (2000) presents a thorough review of the work to date on scalar mixing in turbulent flows. Other reviews on the subject have been provided by Sreenivasan (1991), Shraiman & Siggia (2000), and Dimotakis (2005).

While Equation 1.18 still holds in the turbulent case, the instantaneous velocity components and therefore scalar field vary randomly in both space and time. As discussed in Section 1.2, a Reynolds decomposition can be performed by splitting each instantaneous value into a sum of its mean and a turbulent fluctuation. Equation 1.19 repeats the Reynolds-averaged advection-diffusion equation (1.5) for a passive scalar:

$$\frac{\partial \langle \Theta \rangle}{\partial t} + \langle U_j \rangle \frac{\partial \langle \Theta \rangle}{\partial x_j} = \frac{\partial}{\partial x_j} \left(\Gamma \frac{\partial \langle \Theta \rangle}{\partial x_j} - \langle \theta u_j \rangle \right) . \quad (1.19)$$

As is noted by Webster & Weissburg (2009), the time-averaged description of the passive scalar field hides temporal variations in the turbulent timescale range, which are important to a number of processes. Use of Equation 1.18 must therefore be retained to describe the instantaneous scalar field.

Most large organisms inhabit fluid regimes dominated by turbulent flow, and flows of interest to real-world robotic applications are typically turbulent. As such, the present work on source locating has been restricted to turbulent flows only. Source locating in turbulent flows presents additional challenges, since the information available to the organism or robot – the scalar’s concentration measured within the resulting plume – is inherently patchy and intermittent. The (optionally available) instantaneously measured relative velocity of the fluid to the searcher can also vary widely from its mean value, causing further difficulty.

1.3.2 Source Locating

As previously mentioned, the majority of the relevant research on source locating in turbulent flows has been performed by biologists (e.g., Mafra-Neto & Carde, 1994) or roboticists (e.g., Russel, 1999), with little input from fluid dynamicists, with a few exceptions (Balkovsky & Shraiman, 2002; Vergassola *et al.*, 2007).

Many biological organisms detect and attempt to locate the source of an odourant plume. The odour/chemical (a passive scalar) can be that of food/prey, a sex pheromone emitted by a potential mate, or another biological cue. Significant study has been directed at moths, specifically concerning the males’ upwind search for females by tracing sex pheromones (Mafra-Neto & Carde, 1994). Studies also exist on bacteria, crabs, and sharks, as well as many other organisms (see the references in Webster & Weissburg (2009)). Evidence of long-distance olfactory search patterns by the wandering albatross has also been studied (Nevitt *et al.*, 2008).

As Lo Iacono (2010) and Hayes *et al.* (2002) discuss, a universally optimal search strategy for source location in turbulent environments is not possible. Rather, different algorithms will be better suited to different applications, just as different animals will use differing techniques to locate identical chemical cues in the same environments (Webster & Weissburg, 2009). A selection of the most common approaches is briefly described in the following sections (with discussion oriented towards robotic applications). Figure 1.1 provides a graphical summary of the covered algorithms.

Note that in many cases only binary information on the scalar is employed, meaning that it is either sensed or not, and thus the exact concentration level is only relevant with reference to a given threshold. Also, some algorithms additionally require a wind (fluid) sensor to determine the relative direction of the main flow (velocity information is rarely used).

Most existing source locating algorithms are either bio-mimetic or bio-inspired; in a few cases entirely new algorithms have been proposed such as *infotaxis* (Vergassola *et al.*, 2007), *Lévytaxis* (Pasternak *et al.*, 2009), *fluxotaxis* (Zarzhitsky *et al.*, 2004), and *optimotaxis* (Mesquita *et al.*, 2008). It is noted, however, that even in such cases, final trajectories of the (simulated or real) searchers often resemble those of biological organisms. Certain algorithms, notably *casting* and *spiral-surge*, are widely studied and represent good performance baselines.

Before discussing specific search strategies, it is beneficial to define some common terms in the literature. As summarized by Lo Iacono (2010), a *searcher* is “a biological organism or artificial device which adopts a set of rules in order to locate a source emitting odour in the environment,” and *taxis* is “the orientation of a searcher towards, or away from, the source of a stimulus.” Here, of course, the term odour is synonymous with scalar/contaminant. *Kinesis* refers to an undirected response based solely on the intensity of the scalar cue (Webster & Weissburg, 2009), while a *surge* is

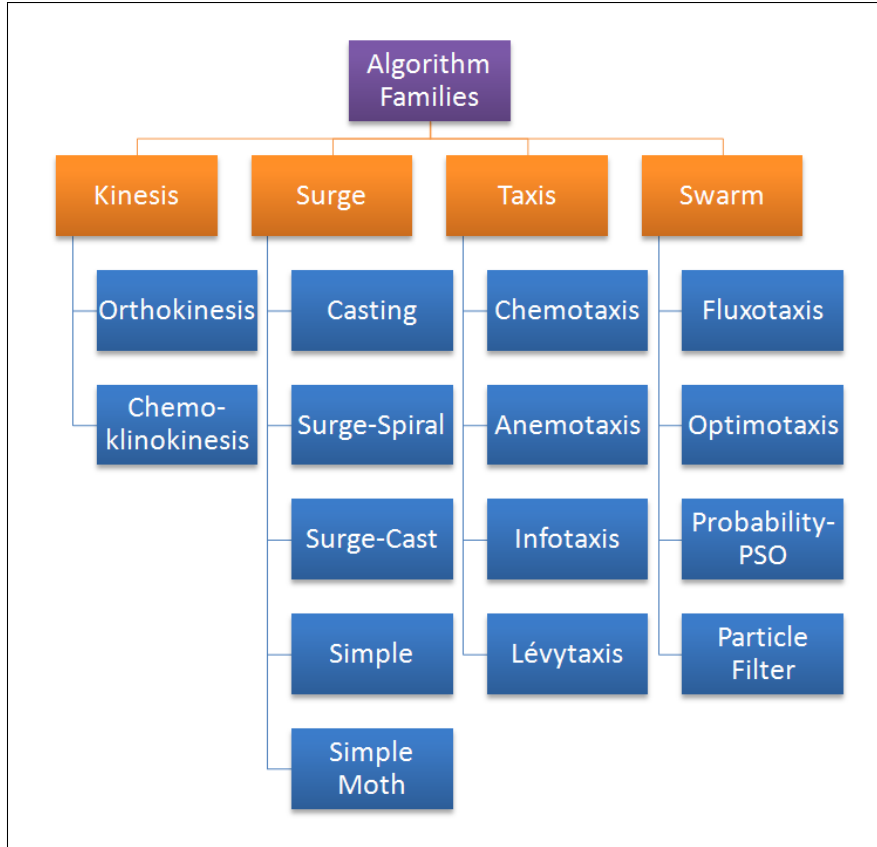


Figure 1.1: Graphical representation of the search strategies discussed in this review, grouped by family. Note that some bridge multiple categories.

a period of upstream-directed travel initiated by a successful acquisition of the plume (Russel, 1999). Lastly, *swarm*-based algorithms rely on two (or many more) searchers working with some degree of collaboration. In the next sections, a cross-section of search algorithms shown in the hierarchal view of Figure 1.1 are summarized.

1.3.2.1 Search Phases

There is consensus in the literature that a given search for the scalar source has either three (Hayes *et al.*, 2002) or four (Li *et al.*, 2001) main but distinct phases. According to Hayes *et al.* (2002), the phases are: i) plume finding – locating the scalar plume within the larger fluid flow, ii) plume traversal – following the plume to its source, and iii) source declaration – ending the search by stating the source is in the

immediate vicinity. Li *et al.* (2001) describe the phases as: i) plume finding (ranging), ii) plume tracing/maintaining (in the upwind direction), iii) plume reacquisition (once the plume has been temporarily exited), and iv) source declaration. These divisions are shown graphically in Figure 1.2.

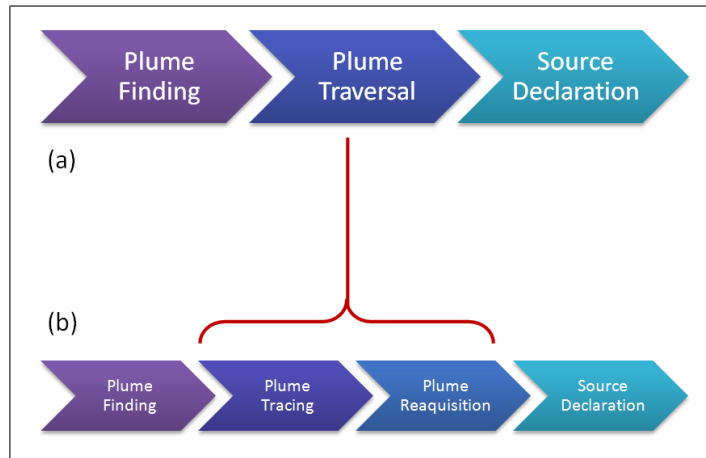


Figure 1.2: Graphical representation of the commonly described search phases. Part (a) is representative of the division originally shown in Hayes *et al.* (2002); part (b) originally from Li *et al.* (2001). It is seen that Hayes’ ‘Plume Traversal’ phase combines the ‘Plume Tracing’ and ‘Plume Reacquisition’ phases of Li.

Most focus has been on the second phase of the search process, that is, plume traversal or plume tracing. Secondary focus has been on the initial plume finding techniques and behaviour. Although the present project aims to incorporate all search phases into a single high-performance algorithm, an understanding of the behaviour of turbulent plumes is most relevant to the second phase (plume traversal).

1.3.2.2 Kinesis-based Algorithms

As seen in Figure 1.3 (reproduced from Webster & Weissburg (2009)), *kinesis* refers to an undirected response based solely on the intensity of the scalar cue. *Orthokinesis* guides the searcher at a speed determined by the cue intensity, while *klinokinesis* guides the searcher via sequential sampling, requiring a memory of at least the last measurement (Webster & Weissburg, 2009).

In a smoothly varying chemical gradient field (i.e., where transport is dominated by diffusion or laminar advection), the most common search strategy is *chemoklinokinesis*, meaning that the searcher’s response is directed up the concentration gradient, but not necessarily perpendicular to it (Webster & Weissburg, 2009). This can be seen in the first half of Figure 1.3. Pure *kinesis*-based algorithms designed to climb the concentration gradient are however not expected to be useful in turbulent and intermittent flows (Masson *et al.*, 2009; Webster & Weissburg, 2009; Lo Iacono, 2010).

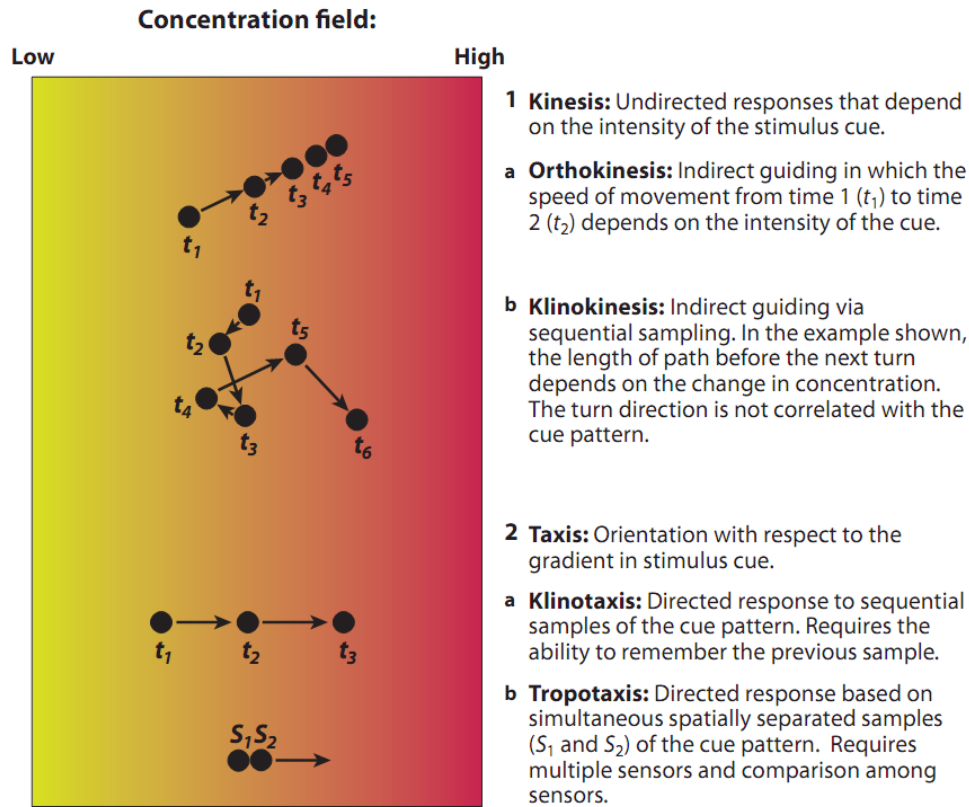


Figure 1.3: Sketch of basic kinesis and taxis search strategies from Webster & Weissburg (2009). *Kinesis* typically occurs in smoothly varying chemical gradient fields, whereas *taxis* can be used in a variety of cue environments (Webster & Weissburg, 2009).

1.3.2.3 Surge-Based Algorithms

Surge-based algorithms are highly bio-mimetic or bio-inspired; most are derived from the work of Russel (1999). The ‘surge’ title describes the primary mode of plume traversal – large upwind surges within the plume, which is in contrast to the motions of the searcher in the plume finding phase. Summarized in the following sections are five of the most used surge-based strategies.

Casting (Zig-Zagging) One of the most common search techniques seen in nature is the *casting* or *zig-zagging* method. The algorithm by Li *et al.* (2001), as implemented by Lochmatter *et al.* (2008) and Lochmatter & Martinoli (2009) in a laminar flow environment, is shown schematically in Figure 1.4. Note that in laminar flow, the plume is effectively a single, continuous filament. However, with appropriate modifications to the algorithm, it can be equally applied to turbulent environments.

Assuming the searcher begins inside of the plume, the robot moves upwind at the angle β until it recognizes that it has left the plume (after a given time, or distance (Li *et al.*, 2001)). It then moves crosswind until a scalar packet of sufficient concentration is detected, at which point it turns and continues the upwind search at the same angle β (Lochmatter *et al.*, 2008). This process is continued until the source declaration phase, which can involve additional criteria.

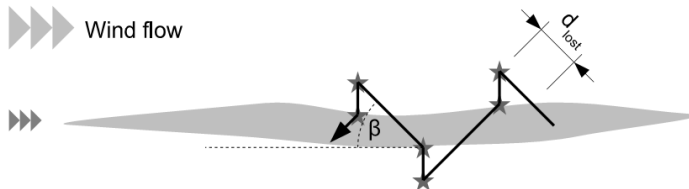


Figure 1.4: Sketch of the *casting* algorithm from Lochmatter & Martinoli (2009). Stars indicate where wind measurements are taken.

The method is experimentally compared to *surge-spiral* by Lochmatter *et al.* (2008) through a standardized set of performance tests examining the efficiency and robustness of the two algorithms. It is also theoretically examined along with the *surge-cast* strategy in Lochmatter & Martinoli (2009). Further comparisons in turbulent flows is done by Li *et al.* (2009), who compare *surge-spiral*, *surge-cast*, and an estimation-based method, using both real robots and simulations.

Surge-Spiral The *surge-spiral* technique, as presented by Hayes *et al.* (2002), can be used for both the plume finding and plume traversal phases (Lochmatter *et al.*, 2008). In the context of plume maintaining (i.e., plume traversal), once the plume has been lost (again, after a given time, or distance (Li *et al.*, 2001)) the robot will move in an Archimidean-type spiral in either the upwind (Lochmatter & Martinoli, 2009) or downwind (Hayes *et al.*, 2002) direction until the plume is reacquired. An upwind ‘surge’ is then performed in the manner of the *casting* algorithm (Lochmatter *et al.*, 2008).

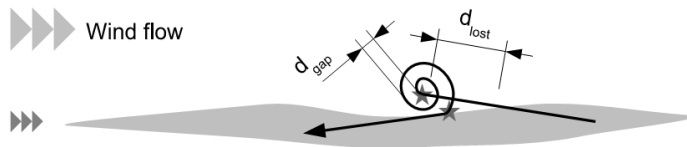


Figure 1.5: Sketch of the *surge-spiral* algorithm from Lochmatter & Martinoli (2009). Stars indicate where wind measurements are taken.

Lochmatter *et al.* (2009) also use the method with real robots in an obstacle-filled laminar flow environment. The introduced obstacles create a turbulent and thus more complex flow downwind, and additional modifications to the strategy are needed (Lochmatter *et al.*, 2009).

Surge-Cast Combining upwind surging with crosswind casting results in the *surge-cast* algorithm as described by Lochmatter & Martinoli (2009). After an upwind surge results in the loss of the plume, the robot will cast orthogonally (crosswind) in both directions until the plume is reacquired before another upwind surge is initiated (Lochmatter & Martinoli, 2009). As shown in Figure 1.6, wind direction measurements are taken at the breaks between the surge and cast phases.

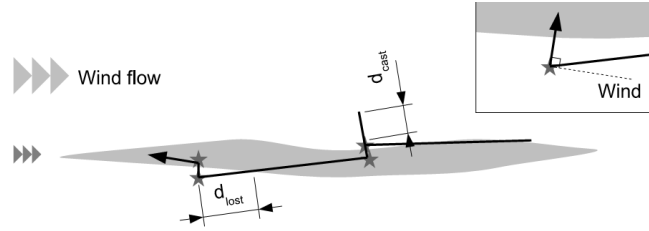


Figure 1.6: Sketch of the *surge-cast* algorithm from Lochmatter & Martinoli (2009). Stars indicate where wind measurements are taken.

Simple Strategy A so-called *simple strategy* was developed by Lo Iacono (2010) which mimics certain insects. When the odour concentration exceeds a cutoff threshold, c_T , an upwind surge is initiated. Otherwise, the searcher makes random crosswind movements. In the two-dimensional case (Lo Iacono, 2010):

$$x(t + \Delta t_{sample}) = \begin{cases} x(t) - u_x \Delta t_{sample} & , \text{ if } c > c_T \\ x(t) & , \text{ if } c \leq c_T \end{cases} \quad (1.20)$$

$$y(t + \Delta t_{sample}) = \begin{cases} y(t) & , \text{ if } c > c_T \\ y(t) \pm u_y \Delta t_{sample} & , \text{ if } c \leq c_T \end{cases} \quad (1.21)$$

This strategy is based on the understanding that a passive search strategy in a turbulent environment is highly inefficient (Balkovsky & Shraiman, 2002). It follows that advancing is always superior, from an efficiency viewpoint, to waiting on station. The

Balkovsky & Shraiman (2002) grid-based analysis further reduces the potential grid points to be visited after a detection (Figure 1.7).

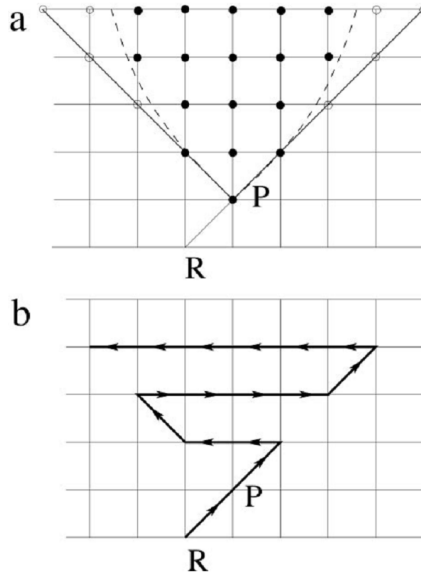


Figure 1.7: Schematic of the Balkovsky search cone regions from (Balkovsky & Shraiman, 2002). The parabolic search domain is set by Equation 1.22; a detection occurs at point R.

Simple Moth Strategy Balkovsky & Shraiman (2002) go further to refine the causality cone region to a slightly smaller, high-likelihood parabolic post-encounter search region (Equation 1.22). Lo Iacono (2010) uses this in his analysis, calling it the *simple moth strategy*; see Figure 1.8.

$$(y - y_i)^2 \leq \frac{4k}{U}(x - x_i) \ln \left[4\pi c_T \frac{k}{U}(x - x_i) \right] \quad (1.22)$$

A comparison of typical search trajectories using the *simple* and *simple moth* strategies, taken from Balkovsky & Shraiman (2002), is shown in Figure 1.9.

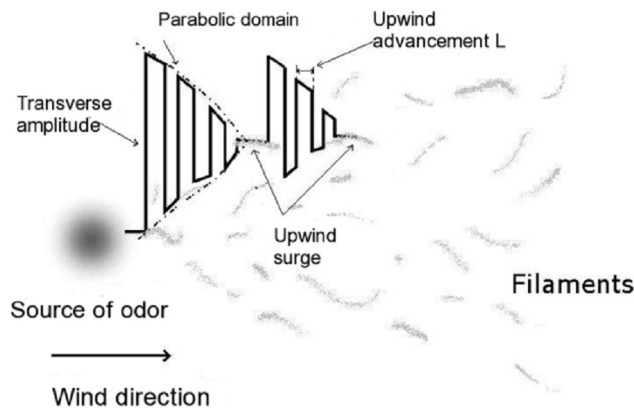


Figure 1.8: Diagram showing a trajectory of the *simple moth* search strategy from Lo Iacono (2010). Note the parabolic high-likelihood search domain.

1.3.2.4 Single Searcher Taxis-Based Algorithms

A large number of *taxis*-based search behaviours exist; the more important ones being discussed in the following sections. New, more complex, search algorithms have also recently been proposed, and are also discussed below. Note that extremely simple tactic methods are shown in the second part of Figure 1.3. Recall that *taxis* is the behaviour of the searcher to orient itself towards the scalar source, where the prefix describes the manner in which this occurs.

Chemotaxis The most basic and widely studied *taxis*-based (or, *tactic*) strategy where the scalar is a chemical is *chemotaxis*. Here, the searcher follows a path determined by the instantaneously measured local gradient. This of course requires two simultaneous measurements to be made. It can be shown (Zarzhitsky *et al.*, 2004) that this strategy will likely fail close to the scalar source if the source creates a time-varying Gaussian-like plume, as is the case in turbulent flows. This is because the gradient tends to zero at the peak (Zarzhitsky *et al.*, 2004). Also, the technique can falsely declare the source at local maxima in certain cases (Zarzhitsky *et al.*, 2004).

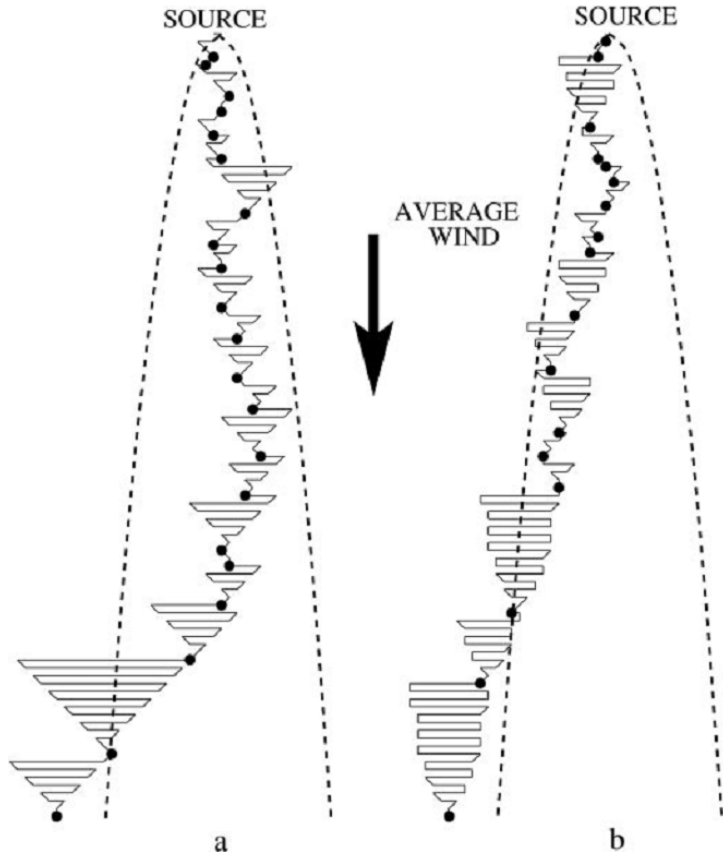


Figure 1.9: Typical search trajectories for causality- and high-likelihood- cones using the *simple moth* search strategy from Balkovsky & Shraiman (2002). The individual parabolic search domain is set by Equation 1.22. Dots indicate detection events.

Anemotaxis The *anemotaxis* strategy has been introduced to overcome these flaws. Knowledge of the fluid flow direction (through a separate sensor) is used to point the searcher upstream. However, in turbulent flows, the instantaneous measurement of flow direction can vary widely from its average, and thus renders the a pure *anemotaxis* technique inappropriate for use in such flows. It can however be useful when used in conjunction with other search strategies.

Infotaxis Vergassola *et al.* (2007) have proposed a new search algorithm called *infotaxis*, where the name is chosen to indicate that each successive movement is made to to maximize the expected rate of information gain. As Martinez (2007)

explains, the time required to finish a search for the scalar source is a function of the entropy of the source distribution. By directing the searcher along a path that maximizes information gain and minimizes the set of possible locations for the source, the *infotaxis* algorithm is highly efficient. Vergassola *et al.* (2007) and Martinez (2007) note that, interestingly, evidence of biological organism-like *casting* and *zig-zagging* motions are seen in the final trajectories. A typical infotactic trajectory in the presence of a mean wind as simulated by Vergassola *et al.* (2007) is shown in Figure 1.10. The algorithm is found to be robust even in turbulent, inhomogeneous flow (Vergassola *et al.*, 2007).

An interesting extension of the *infotaxis* work of is provided by Barbieri *et al.* (2011). They note that the infotactic strategy could be particularly useful for fully three-dimensional searches. Algorithms such as *casting*, *zig-zagging*, and random walks are all space-filling in the planar (2D) case, but not in 3D (Barbieri *et al.*, 2011). Masson *et al.* (2009) also examine the algorithm, as implemented by a team of searchers.

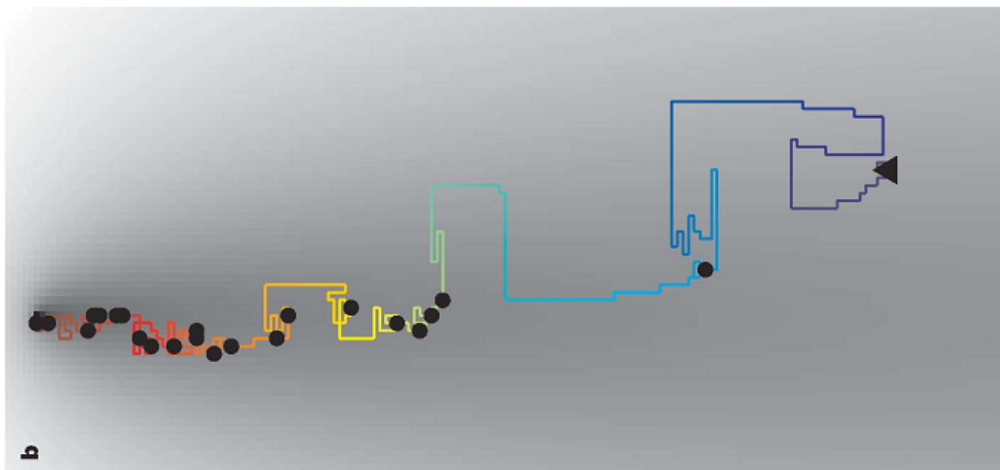


Figure 1.10: Typical *infotaxis*-based search trajectories in the presence of a mean wind (from left) from Vergassola *et al.* (2007). The grayscale is representative of the scalar concentration; detection events are noted by black dots.

Lévytaxis Pasternak *et al.* (2009) introduce a novel bio-inspired search strategy

called *Lévy taxis* as a way to overcome the issues with the spatial and temporal intermittency of the scalar plume. The term is based on the type of ‘walk’ used in plume finding, and the algorithm is particularly well suited to the plume finding phase of the search in vast, cue-less regions (Pasternak *et al.*, 2009). During the search, the turning angles are sampled from a wrapped Cauchy distribution centered on the upstream angle ($0 \leq \rho \leq 1$) (such that a move upstream is more likely), and the move lengths are extracted from a Lévy (power-law) distribution with $1 < \mu \leq 3$ (Pasternak *et al.*, 2009). In the paper, this type of walk is compared through simulation to other pure ones such as Brownian-, Lévy- and correlated random walks, as well as the deterministic *casting* strategy. The *Lévy taxis* algorithm is found to provide an optimal balance of efficiency and accuracy (Pasternak *et al.*, 2009).

1.3.2.5 Swarm Taxis-Based Algorithms

Although the present work only deals with algorithms using one searcher, certain search algorithms draw inspiration from the collaborative nature of insect and fish swarms. For example, Hayes *et al.* (2002) looked at control algorithms using swarm intelligence applied to the standard *spiral-surge* algorithm, inspired by social insects. Using both real and simulated robots, they showed that employing swarm intelligence in the source locating task increased efficiency, while still only using simple sensory information and reactive behaviour (Hayes *et al.*, 2002).

Fluxotaxis A rigorously evaluated *fluxotaxis* search algorithm has been proposed by Zarzhitsky *et al.* (2004). The strategy is fundamentally swarm-based, and tactic in nature. The underlying idea is that by using multiple searchers (arranged to form a robotic ‘lattice’) to calculate the local divergence of the scalar mass flux, its gradient can be followed in the sharpest increasing direction all the way to the source (Zarzhitsky *et al.*, 2004). Zarzhitsky *et al.* (2004) mathematically prove the robustness

of the strategy in different one-dimensional flow cases, using two (communicating) searchers and assuming a Gaussian plume distribution. Under the studied conditions, it is shown to be an efficient and robust swarm-based algorithm.

Optimotaxis Another *taxis*-based swarm strategy is the suggestively named *optimotaxis* search algorithm proposed by Mesquita *et al.* (2008). Each individual searcher can take only instantaneous point measurements, and is not able to measure its position within the search domain. The algorithm is bio-inspired (from chemotactic bacteria), in that the non-communicating swarm elements are individually guided by a biased random walk (similar to the random walks compared in Pasternak *et al.*, 2009) (Mesquita *et al.*, 2008). Again, since local gradient information is either unavailable or unreliable in the turbulent environment, a pure *chemotaxis* approach is not viable. A ‘supervisor’ watches the swarm converge to the spatial probability density of the scalar source itself; both local and global maxima can be found by this method (Mesquita *et al.*, 2008).

Probability-PSO Algorithm The problem of source locating within turbulent, ventilated indoor environments is investigated through simulation by Li *et al.* (2008). The nature of the boundary conditions means that as well as the cues being patchy and intermittent, longtime local maxima can exist (i.e., in corners; Li *et al.*, 2008). Again, a swarm *taxis*-based algorithm is suitable here, where individual searcher movements are driven through a combination of *anemotaxis* and binary odour information. Li *et al.* (2008) suggests the P-PSO (probability-particle swarm optimization) algorithm, again to help overcome the issue of falsely declaring the local maximum of the scalar as its original source. With each search step an updated probability map is generated through Bayesian interference to guide the next movements of every searcher (Li *et al.*, 2008).

Particle Filter Algorithm A team of (real) robots in outdoor airflow is studied by Li *et al.* (2011) using a particle filter algorithm. Here once again, distributing the odour source localization task among multiple searchers employing the *spiral-surge* algorithm of Hayes Hayes *et al.* (2002) (which uses simultaneously a binary measurement of the scalar and a relative-wind velocity value), and particle-filtering to update an estimated probability map of the source location (Li *et al.*, 2011). The experimental results are compared, and found superior to a pure Bayesian interference method (Li *et al.*, 2011). It is noted that Hayes *et al.* (2002) originally examined swarms of real (and simulated) robots in tests of a collaborative *spiral-surge* algorithm.

1.4 Thesis Objectives and Overview

1.4.1 Thesis Objectives

The primary objective of present work is to increase the efficiency and accuracy of locating a scalar source emitted in a turbulent flow, by incorporating knowledge of turbulence. By applying an understanding of the behaviour of turbulent scalar plumes, it will be possible to design more intelligent source locating algorithms. These algorithms will furthermore be tested in a turbulent channel flow facility, in order to evaluate their real-world performance. It is also hoped that the present work will provide the input often requested by other researchers in the field (Settles, 2006; Webster & Weissburg, 2009). As can be seen in the literature review, the goal of designing a simple, efficient, and robust algorithm for scalar/contaminant source locating in turbulent flows is a challenging pursuit, and will provide many avenues for future research.

1.4.2 Thesis Overview

This thesis encompasses five chapters. Chapter 2 discusses the experimental setup and data acquisition methods. Detailed information on the experimental facility, scalar injection method and traversing mechanism setup, along with the measurement and data acquisition techniques and calibration will be presented therein.

Chapter 3 provides an overview of the flow validation and experimental conditions in the channel. The physical integrity of the channel, one-dimensionality of the velocity field, and passivity of the scalar field are discussed and the precise experimental conditions are given.

Chapter 4 contains the results of the present work and discusses them in the context of the existing literature. Results from measurements of the scalar field and its evolution are shown, along with a detailed description of the algorithm development process. Final results from both the one- and two-dimensional searches are presented, as well as a discussion of the developed two-dimensional scalar plume model.

Finally, Chapter 5 presents conclusions and suggested future directions for the project. A complete bibliography of cited works completes this thesis.

Chapter 2

Experimental Setup

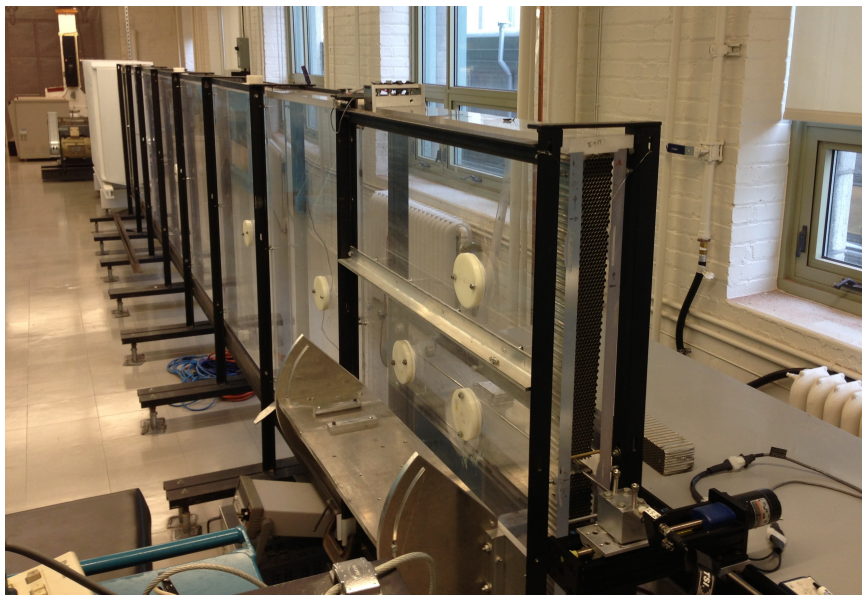


Figure 2.1: Channel used in the present work as seen obliquely from the test section end.

All experiments for the present work were conducted in the high-aspect-ratio channel (shown in Figure 2.1) in the McGill University Aerodynamics Laboratory. Velocity and scalar measurements were recorded in the test section, wherein the flow was fully developed and turbulent. The measurements were made using hot-wire anemometry and cold-wire thermometry systems, respectively. The experimental apparatus and measurement techniques are described in this chapter.

2.1 The Wind Tunnel

The design and construction of the wind tunnel is discussed in an honours thesis by McLeod (2000). Detailed specifications and characteristics can be found therein. Furthermore, Lavertu (2002) and Costa-Patry (2005) used the apparatus in their masters' work.

The wind tunnel is of an open-circuit, blower design. It is composed of i) a blower unit, ii) flow conditioning elements, and iii) the test section. The blower unit comprises a Hudson Buffalo centrifugal blower powered by a 5.6 kW (7.5 hp) synchronous AC motor. The motor is driven by an ABB ACS 600 frequency converter control unit, allowing precise control of the motor and fan assembly's speed (rpm) and thus the air flow rate through the channel. Filters at the blower inlet prevent contamination of the flow by particles larger than $0.3\ \mu\text{m}$, which can adversely affect the sensitive measuring instruments. To reduce system vibration, the motor and blower are mounted on rubber pads and a flexible joint is used to connect the blower outlet to the flow conditioning section inlet.

The flow conditioning section serves to remedy the irregular flow exiting the blower (which has an exit cross-section of $0.45 \times 0.33\ \text{m}^2$) before it reaches the test section. Five flow-conditioning elements are employed in this process: i) a perforated plate at the blower exit, ii) a 45° diffuser with four screens positioned inside (to prevent separation that would otherwise occur in a such a high-angle diffuser, by balancing out the pressure rise (McLeod, 2000)), iii) an aluminum honeycomb section in the settling chamber, iv) six appropriately located screens following the honeycomb section, and v) a contraction. Two rods (3.2 mm in diameter), placed 3 mm away from the channel walls and 60 mm downstream from the flow conditioning section exit, trip the boundary layer to aid in quickly developing the flow in the channel. In addition to these upstream flow conditioning elements, a 10 cm piece of aluminum honeycomb

flow-straightener is also included at the exit of the test section to minimize the effect of external flow disturbances on the flow within the test section.

The channel test section is 8 m long, 1.1 m tall, and 0.06 m (60 mm) wide. The high aspect ratio (18.3) is sufficiently large to ensure that the top and bottom walls do not appreciably affect the flow at the center of the channel, thus creating a two-dimensional flow field where measurements are made. The channel walls are constructed from plexiglass sheets, nominally 25.4 mm (1 in) thick, joined by “biscuits.” By adjusting a number of bolts positioned between the steel supporting frame and the plexiglass sheets, the “steps” at each individual interface between two plexiglass sheets can be kept smaller than 5 viscous lengths (approximately 0.15 mm for the present work), as recommended by Tennekes & Lumley (1972) to ensure that the walls can be considered hydrodynamically smooth. The part of the test section wherein all experiments were performed is located 7 m downstream of the flow conditioning section exit, and is $1 \times 1.1 \times 0.06 \text{ m}^3$ in size. The flow in this region of the channel is fully developed and turbulent (Lavertu, 2002). Four circular ports are installed in the test section; the first (port 8-1) is 7.33 m downstream, and the second, third, and fourth (ports 8-2A, 8-2B, and 8-2C) are 7.67 m downstream. Port 8-2B is located at the centreline, while ports 8-2A and 8-2C are located 0.275 m above and below, respectively (see Figure 2.2). Only ports 8-1 and 8-2B were used in the present work.

For the one-dimensional (1D) search domain experiments, the probe was inserted through a special centre-bored plug at the desired port location. Other ports were fully plugged to ensure smooth walls within the channel. In the two-dimensional (2D) search domain experiments, all ports were fully plugged and the probe was inserted through a break in the honeycomb flow straightener at the exit of the test section.

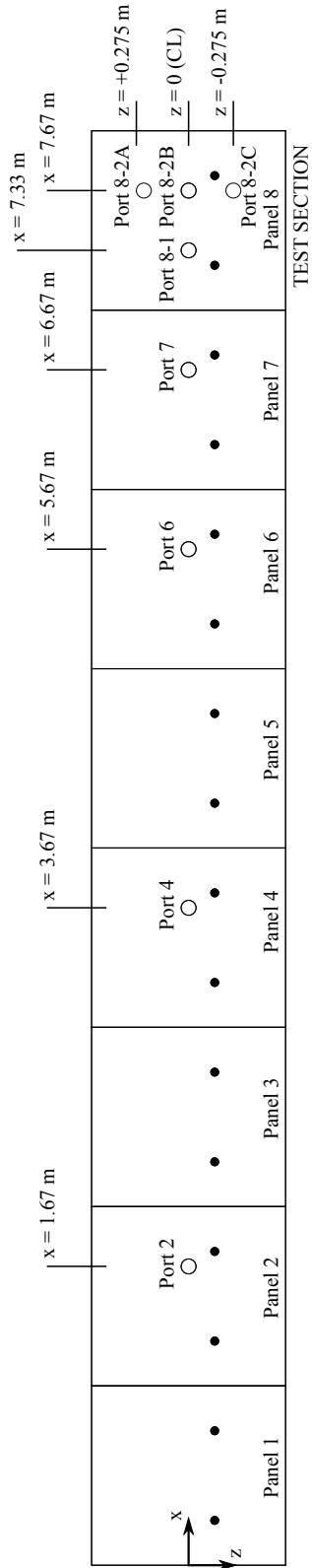


Figure 2.2: Channel port locations. Filled circles are pressure taps only; open circles are measurement ports. Note the test section is panel 8. Not to scale.

2.1.1 Coordinate System

A schematic of the test section is shown in Figure 2.3, showing also the coordinate system definition. A top view of the test section is presented in Figure 2.4. The x -axis is parallel to the streamwise direction, with its datum located at the line source (see next section). The x -coordinate is thus a measure of the downstream distance from the source, and not an absolute position in the channel. The y -axis is aligned in the cross-stream direction, with datum at the wall opposite from the traversing mechanism. As such the y -coordinate is an absolute measure of distance from the wall. The z -axis is spanwise/vertical with datum at the channel centreline, and is aligned with the gravitational vector. All measurements were taken at the spanwise centreline ($z = 0$).

2.1.2 Scalar Source

The scalar (in the present work, a small temperature excess) was injected into the flow by means of a heated line source mounted vertically in the channel (along the z -axis), held in position by aluminum plugs in the plexiglass top and bottom walls. Within each aluminum plug, 0.3 mm diameter glass capillary tubes provide electrical isolation from the plug. Depending on the nature of the experiment, one of two different diameter Nichrome wire line sources was powered by a Kepco constant current/constant voltage DC power supply, accurate to within 0.01%. For the 1D search domain the smaller (0.127 mm diameter) wire was employed, powered at 45 W m^{-1} . This was achieved with 70 V and 0.6 A, and was monitored throughout the experiments.

For the 2D search domain, measurements taken farther downstream require the larger (0.254 mm diameter) wire, powered at 100 W m^{-1} (approximately 54 V and 2.0 A) to achieve an adequate signal-to-noise ratio. A 100 g free weight attached at the

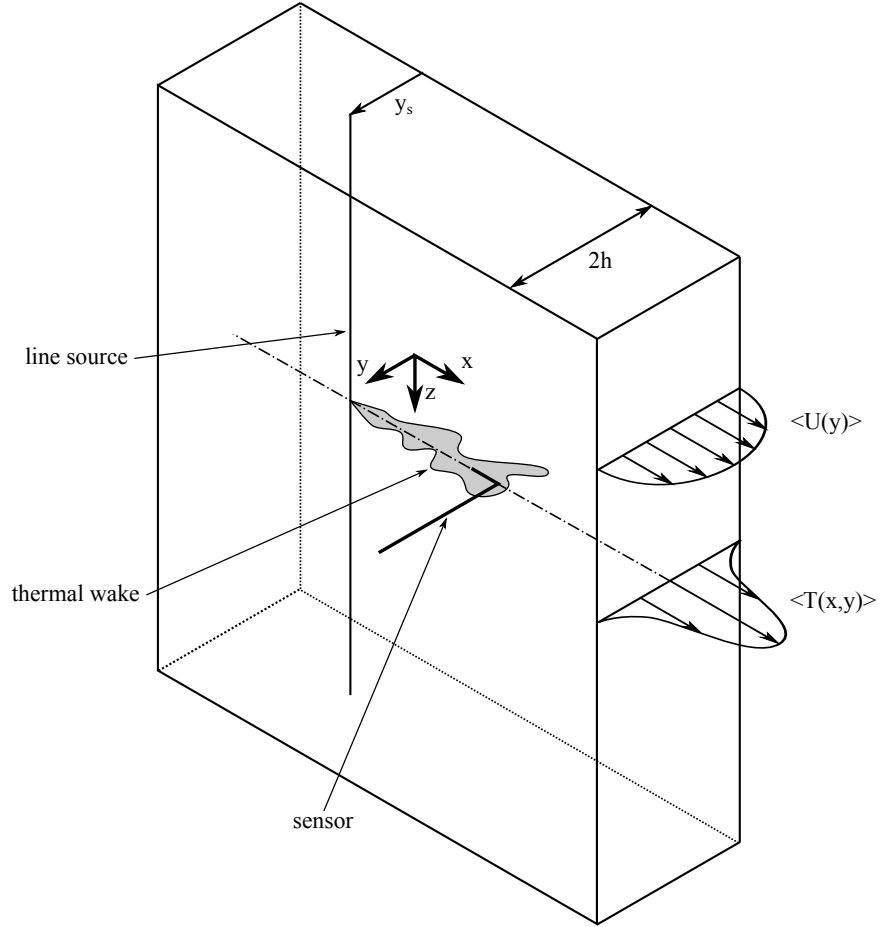


Figure 2.3: Schematic of the test section, showing coordinate system definition. Note the gravity vector is downward, and the y -datum is on the back wall. Not to scale.

bottom of the Nichrome wire allows for thermal expansion of the source without sagging.

All experiments were performed with the line source located at $y_s/h = 1.0$, where $h = 0.03$ m is the channel half-width. The nominal cross-stream domain is bounded by $y/h = [0, 2]$, while the downstream domain is limited to $x/h = [0, 25]$. Further reductions in the measurement domain occurred due to physical constraints (e.g., finite width of the probe, etc.).

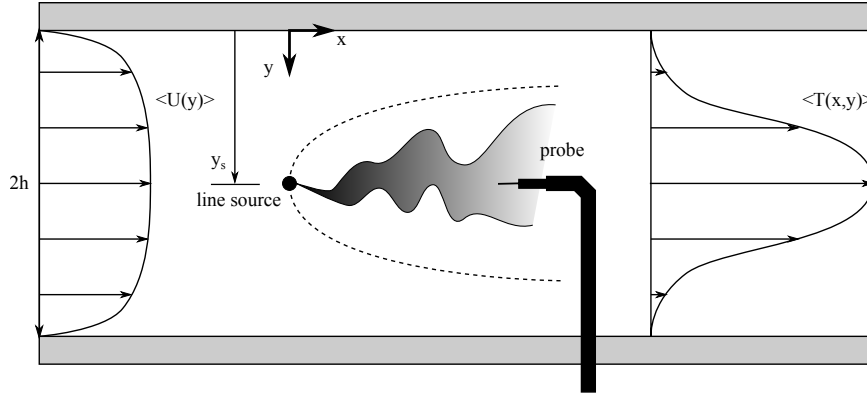


Figure 2.4: Top view of the experiment. Solid line: instantaneous thermal wake; Dashed line: time-averaged wake. Line source size is exaggerated for clarity. Not to scale.

2.1.3 Traversing Mechanism

For the 1D experiments, a single Velmex BiSlide traversing mechanism, driven by a NEMA 34 stepper motor, was used to move the probe in the cross-stream (y) direction. It was controlled by one channel of a Velmex VXM-2 stepper motor controller, allowing for a positional accuracy of 0.01 mm in the y -direction, though all traverses were done in 0.1 mm steps. The x - and z -positions were fixed for the 1D experiments.

In the 2D case, a second Velmex BiSlide traversing mechanism was used to support the first unit at a 90° angle, which allowed movement in the x - y plane. Both channels of the stepper motor controller were employed in this case. Again, all traverses were done with steps of 0.1 mm. The 2D setup is shown in Figures 2.5 and 2.6.

2.2 Measurement Techniques

All data was collected using either hot-wire anemometry (HWA), or cold-wire thermometry (CWT). These techniques have high frequency response, provide good signal-to-noise ratios, and are able to resolve spatial and temporal scales on the order of

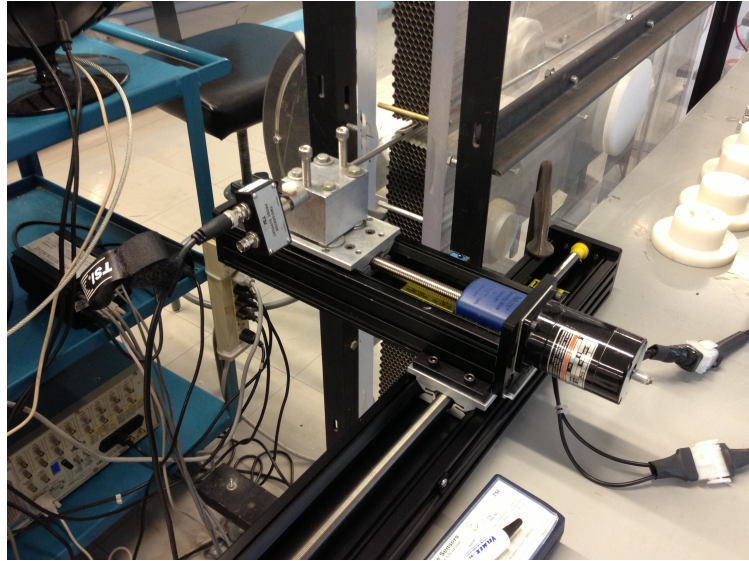


Figure 2.5: The 2D traversing mechanism setup. Note that the x - and y -directions appear reversed from the schematic below due to the picture angle.

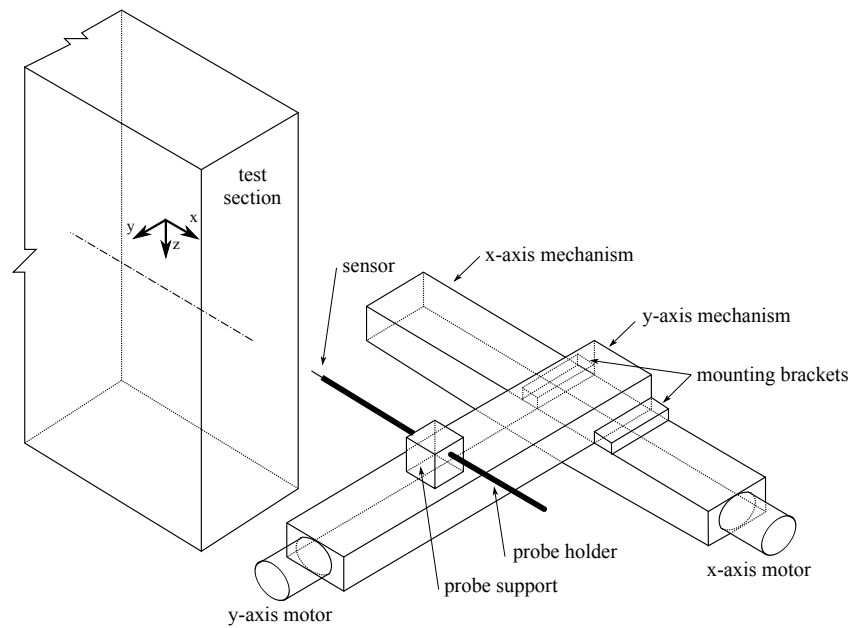


Figure 2.6: Schematic of the 2D traversing mechanism setup. Not to scale.

the Kolmogorov microscales for the present flow. HWA, CWT, and calibration techniques specific to the present work are discussed in the following sections, as is data acquisition and signal conditioning.

2.2.1 Probe Setup

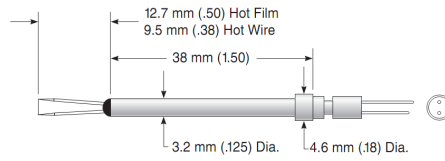
The hot- and cold-wire probe systems was mounted on the same equipment. This consisted of i) the probe itself, a TSI Model 1210 General Purpose Probe or TSI Model Model 1218 Boundary Layer Probe for near-wall velocity measurements, ii) a 90° TSI Model 1152 Angle Adapter (when the TSI 1210 probe was used in the 1D searches), and iii) a TSI Model 1150 Standard Probe Support. The whole assembly was supported in a TSI Model 1158 Locking Protective Shield, which was in turn mounted to the Velmex BiSlide traversing mechanism. The parts' schematics and descriptions are extracted from the TSI catalogue and shown in Figure 2.7.

2.2.2 Hot-Wire Anemometry

Streamwise (longitudinal) velocity measurements in the channel were made using a hot-wire anemometer. The probe consists of a 0.5-mm-long, 3- μm -diameter tungsten wire suspended between two prongs, oriented normal to the mean flow in the spanwise direction. The probe was constructed by first soldering a length of wire to the prongs, then etching away (with nitric acid) the protective copper cladding in the desired region, resulting in a length-to-diameter ratio of approximately 200. Its resistance at ambient temperature was about 5 Ω .

With the overheat ratio set to 1.8, a TSI IFA 300 constant-temperature anemometer (CTA) heated the tungsten wire to approximately 250 °C (Bruun, 1995). Because the resistance of the wire was held constant, a change in the air velocity over the sensor

Model 1210 General Purpose Probe

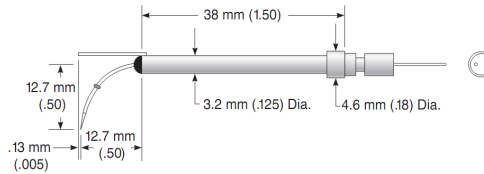


Recommended Sensors

For Gas Applications
 1210-T1.5
 1210-20
 Max. Fluid Temp. = 150°C
For Liquid Applications
 1210-20W

(a) TSI Model 1210 General Purpose Probe.

Model 1218 Standard Boundary Layer Probe

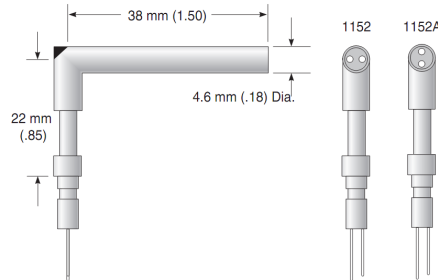


Recommended Sensors

For Gas Applications
 1218-T1.5
 1218-10
 1218-20
 Max. Fluid Temp. = 150°C
For Liquid Applications
 1218-20W

(b) TSI Model 1218 Standard Boundary Layer Probe.

Model 1152 90° Angle Adapter

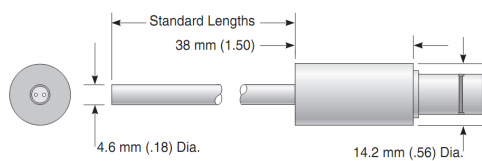


Right angle bend provides access to upstream points with straight probes.

Specify
 1152
 1152A

(c) TSI Model 1152 Angle Adapter.

Model 1150 Standard Probe Support

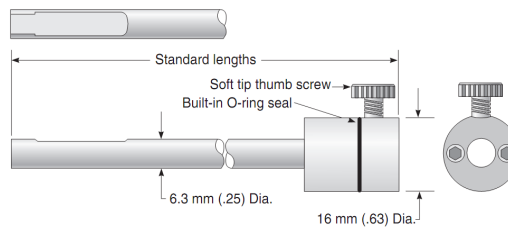


Designed for most standard TSI single sensor plug-in probes.

Specify
 1150-6 for 152 mm (6 in.) length
 1150-18 for 457 mm (18 in.) length
 1150-36 for 915 mm (36 in.) length
 Max. Fluid Temp. = 150°C

(d) TSI Model 1150 Standard Probe Support.

Model 1158 Locking Protective Shield



Protects probe when used as a shield, locks probe into socket when extended. Provides sturdy support for probe. Fits Model 1150 Probe Supports and most standard probes.

Specify
 1158-6 for 152 mm (6 in.) length
 1158-18 for 457 mm (18 in.) length
 1158-36 for 915 mm (36 in.) length

(e) TSI Model 1158 Locking Protective Shield.

Figure 2.7: TSI probe equipment, extracted from the manufacturer's catalogue.

resulted in a variation of the voltage required to maintain the constant resistance. This relationship was used to generate a calibration curve when the air velocity was precisely known.

2.2.2.1 Hot-Wire Calibration

To calibrate the hot-wire probe, a TSI Model 1127 Laminar Calibration Jet was used (see Figures 2.8 and 2.9). The wire must first be “burned-in,” and was left in the jet for 24 hours while operating. During the subsequent calibration, by regulating the air supply pressure (which was measured by a high-accuracy MKS 220D pressure transducer), the (known) velocity of the laminar jet was varied. The square of the output signal of the CTA (E^2) is plotted as a function of flow velocity (U) in Figure 2.10 for probe SN105-06b. A modified King’s Law curve was fitted (Equation 2.1) by least-squares regression. The constants for this particular probe were: $A = 11.113$, $B = 3.8234$, $n = 0.44646$, and the correlation coefficient was $R = 1.0000$. The calibration was performed at or very near the typical ambient temperature of the experiments to minimize errors arising from changes in the freestream temperature. Note also that more data points were recorded at lower velocities, since the curvature of the calibration curve is higher there (Bruun, 1995).

$$E^2 = A + B \cdot U^n \tag{2.1}$$

2.2.3 Cold-Wire Thermometry

All fluctuating temperature measurements were done using cold-wire thermometry. Although mounted on the same TSI probe equipment, the sensor was made from an approximately 0.5-mm-long, 0.625- μm -diameter piece of Wollaston wire. This gave



Figure 2.8: The laminar calibration jet. Note that the air source and main shutoff valve shown in the schematic below are not seen in the picture.

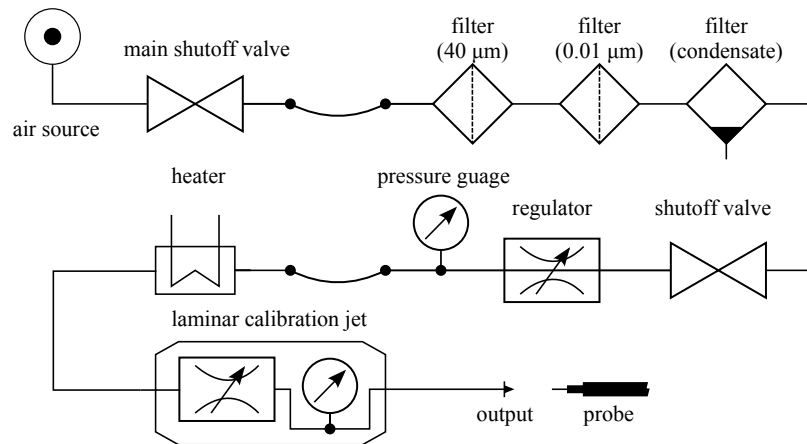


Figure 2.9: Schematic of the laminar calibration jet. Not to scale.

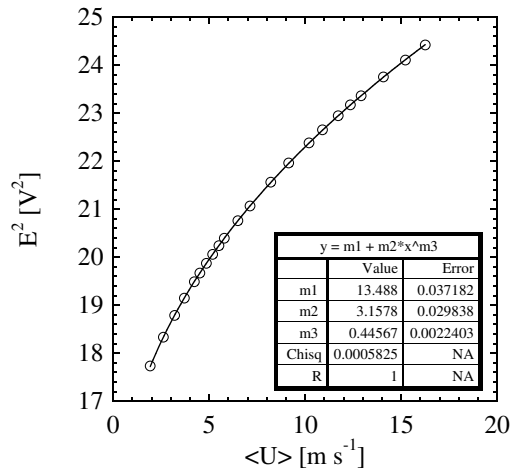


Figure 2.10: Hot-wire calibration curve for 3 μm velocity probe SN105-06b.

a length-to-diameter ratio of 800, and a resistance of approximately 150Ω . Similar to the construction methods for the HWA probes, the protective silver cladding was etched away to reveal the desired length of platinum core.

A constant-current anemometer (CCA) used in the present experiments as a CWT was manufactured at Université Laval in Québec. It passes a $100 \mu\text{A}$ current through the wire. Since the resistance of the cold-wire probe changes linearly with small changes in temperature, the output voltage of the CCA changes linearly with temperature as well. This relationship can be used to generate a calibration curve relating the output voltage to flow temperature.

2.2.3.1 Cold-Wire Calibration

Cold-wire calibration was performed in the same TSI 1127 laminar calibration jet. Here, the air velocity was fixed at 5.0 m s^{-1} , which was near that of the experiments. The air flow temperature was varied by means of three 120 W electric heating elements upstream of the calibration jet. A linear relationship between temperature (T) and

output voltage (E) (Equation 2.2) was fit to the calibration data using least-squares regression. To improve the quality of the calibration, the flow was first heated up to a maximum temperature of approximately 80 °C and then the heaters were turned off. Measurements were recorded at 0.5 °C increments, starting at about 8 °C above ambient temperature. Figure 2.11 presents a representative calibration for probe SN205-03.

$$T = C \cdot E + D \tag{2.2}$$

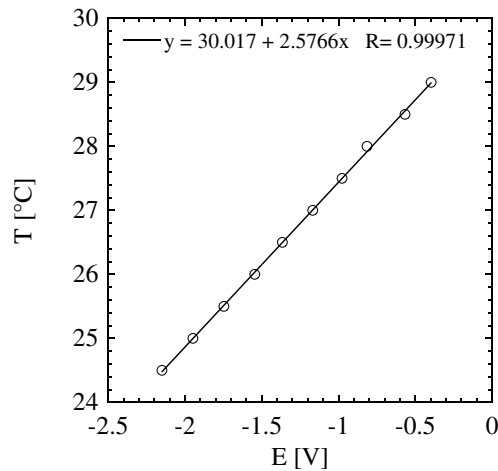


Figure 2.11: Cold-wire calibration curve for 0.625 μm temperature probe SN205-03.

2.2.4 Mean Ambient Temperature Measurement

Mean ambient temperature measurement was made using the same CW probe, moved to an *a priori* known location far from the scalar plume. Data was recorded to determine the ambient background statistics of the mean temperature and root-mean-square temperature fluctuation. This allowed the removal of the freestream temperature T_∞ from the raw search data to determine the mean temperature excesses

$(\langle T \rangle - T_\infty)$.

2.2.5 Spatial and Temporal Resolution

Since the flow in the channel was turbulent, a large range of scales in both the velocity and temperature fields was present and of interest. As such, the probes were required to be smaller than the smallest length scale of the flow, and have smaller time constants (i.e., faster frequency response) than its smallest time scales. The scales in question are the Kolmogorov microscales of length and time, defined in Equations 2.3 and 2.4 respectively, and are further discussed in Chapter 3.

$$\eta \equiv \left(\frac{\nu^3}{\epsilon} \right)^{\frac{1}{4}} \quad (2.3)$$

$$\tau \equiv \left(\frac{\nu}{\epsilon} \right)^{\frac{1}{2}} \quad (2.4)$$

Here, ϵ is the dissipation rate of turbulent kinetic energy and ν is the kinematic viscosity of the fluid. Note that since the Prandtl number $Pr = \nu/\alpha$, where α is the thermal diffusivity of the scalar, is on the order of one (0.71 for air at the conditions under consideration), the hydrodynamic and scalar microscales are almost equal.

2.2.5.1 Spatial Resolution

Since the length of the hot- and cold-wire probes was 0.5 mm, this placed a limit on the spatial resolution of the probes. As will be seen in Chapter 3, it was slightly larger than the Kolmogorov microscale of length. However, these probe sizes had length-to-diameter ratios that provided a good balance between an acceptable signal-to-noise

ratio within the measuring equipment, and spatial resolution.

2.2.5.2 Temporal Resolution

The cold-wire time constant of the probe was measured to determine the frequency cut-off, $f_c = 1/(2\pi\tau_{cw})$, of the wire and thus ensure the temporal resolution of the probe is sufficient. By the method of Lemay & Benaissa (2001), a square-wave signal was passed through the probe to accomplish this. The output of the CCA (an example of which is plotted in Figure 2.12) was fit to the model of Lemay & Benaissa (2001) (Equation 2.5) to determine the time constant of the cold wire, τ_{cw} .

$$E = C_1e^{-t/\tau_E} + C_2e^{-t/\tau_{cw}} + C_3 \quad (2.5)$$

The electronics time constant ($\tau_E = 3 \mu\text{s}$) is known *a priori* and the constants C_1 , C_2 , and C_3 were determined. f_c was found to be in the order of 4 – 5 kHz for the probes built. This was sufficiently above the Kolmogorov frequency microscale of the flow studied. The frequency microscale in this case is defined more restrictively by the Kolmogorov microscale of length and the longitudinal mean velocity, i.e., $\langle U \rangle / (2\pi\eta)$, rather than the inverse of the Kolmogorov microscale of time ($1/\tau_\eta$). Note that, as the frequency response performance degrades over time due to contamination of the wire, the probe was occasionally cleaned in isopropyl alcohol.

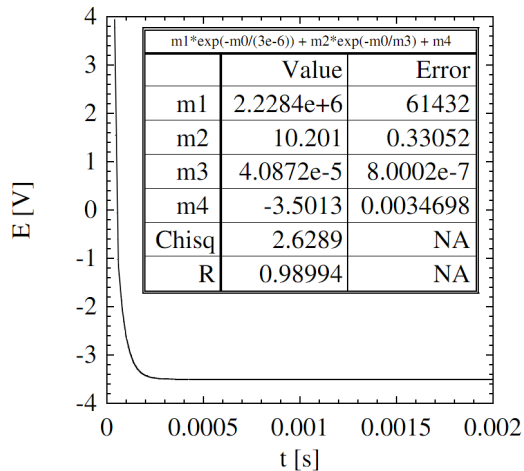


Figure 2.12: Cold-wire time constant calibration curve for 0.625 μm temperature probe SN205-03.

2.3 Data Acquisition

2.3.1 Hot-Wire Measurements

The hot-wire probe was connected to the input of a TSI IFA 300 anemometer by a 5 m coaxial BNC cable. The output of the HWA was passed through a Krohn-Hite Model 3382 48 dB/decade Butterworth band-pass filter. The signal was both low-pass filtered (to remove high-frequency noise), and high-pass filtered (to remove any drift in the mean values). The low-pass frequency f_{LP} was found and set at every measurement point by examining an unfiltered dissipation spectrum, and was in the range of 2 – 5 kHz. By the Nyquist criterion, to prevent aliasing, the sampling frequency was set to twice f_{LP} for spectra data. The high-pass frequency f_{HP} can be chosen by examining an unfiltered energy spectrum. The frequency (below the integral frequency) at which the spectrum approaches zero represents the point at which there is no significant turbulent kinetic energy present. However, since the convergence of measured spectra at the frequency range in question (around 0.05 Hz)

is very slow, f_{HP} was set to 0.1 Hz for all measurements.

2.3.2 Cold-Wire Measurements

The cold-wire probe was connected to the input of the CCA. Gain, offset, and dynamic compensation were all adjusted on the CCA. The output signal was passed to the same Krohn-Hite filter, and again both low- and high-pass filtered. The low-pass filter was set to approximately 10 kHz to resolve all scales. The high-pass filter was again set to 0.1 Hz.

2.3.3 Analogue to Digital Conversion

For both HWA and CWT measurements, two separate signals were fed into the National Instruments PCI-6036E DAQ board: i) the low-passed only signal (with mean intact), and ii) the band-pass filtered and amplified signal containing only the fluctuations. The signals went through a 16-bit analog-to-digital conversion process which quantizes the signal between ± 5 V. Time-series data of both signals was recorded using a LabVIEW Virtual Instrument (VI). The VI produces data files that were then analysed using custom FORTRAN and MATLAB software to translate the voltages into velocities or temperatures, and/or perform statistical calculations. During all experiments, both signal channels were monitored on a Tektronix TDS1000B digital oscilloscope.

For some measurements, a 20 dB (10X) gain on the band-pass filtered data was employed to improve the usage of the DAQ card's sampling range. For example, a typical velocity signal may be 4.5 ± 0.4 V, so removal of the mean by high-pass filtering (leaving only the fluctuating signal) and then amplifying the signal is a better use of the card's range, which in this case is ± 5 V.

Chapter 3

Flow Validation and Experimental Conditions

The experimental conditions under which the present work was completed are discussed in this chapter. Validation of the major assumptions underlying the work will also be presented.

3.1 Flow Validation

The present work assumes the following:

1. The velocity field is one-dimensional and fully developed in the test section.
2. The scalar is passive (i.e., has no dynamical effect on the fluid motion).
3. The scalar field is independent of the source diameter (for the downstream measurement locations studied herein).
4. The scalar field is two-dimensional (i.e., independent of the z -direction).
5. The channel walls are adiabatic.

These assumptions are discussed in the sections below. Given that the identical flow to the one studied herein was examined in detail by both Lavertu (2002) and Costa-Patry (2005), references to their flow validation methods and results will be frequently made.

3.1.1 Fully Developed, One-Dimensional Channel Flow

3.1.1.1 Physical Integrity of the Channel

It is assumed the flow in the test section is fully developed and one-dimensional (i.e., the flow field varies only in the wall-normal (y) direction). Though this was verified by McLeod (2000), Lavertu (2002), and Costa-Patry (2005), there was concern that renovations in the Aerodynamics Laboratory during 2010-2011 had affected the channel alignment and thus the nature of the flow. As such, each plexiglass panel was checked, adjusted, and re-checked to i) minimize discontinuities at the interfaces, and ii) ensure a constant 60 mm channel width (with a stricter tolerance in the test section) using a digital depth gauge and a special arrangement of the traversing mechanism. The final results of this adjustment are shown in Table 3.1.

Table 3.1: Channel width measurements.

Port	x (m)	Width (mm)	Error (mm)
2	1.67	60.10	± 0.025
4	3.67	60.05	± 0.025
6	5.67	59.90	± 0.025
7	6.67	60.05	± 0.025
8-1	7.33	60.025	± 0.0125
8-2B	7.67	60.050	± 0.0125

Additional measurements were also made using a laser sight to determine the radii of curvature for different sections of the channel, since a minor spanwise curvature in the channel (about its z -axis) is possible due to its length (8 m). Using two slotted cards

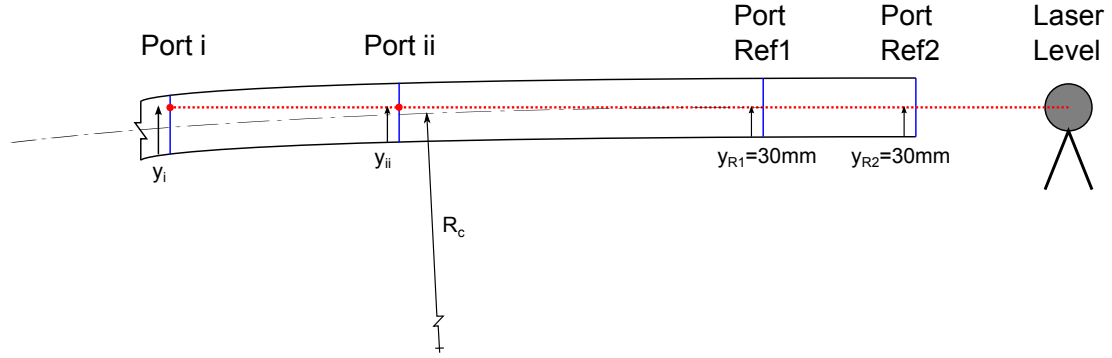


Figure 3.1: Channel curvature measuring setup. Blue lines indicate slotted cards inserted into the reference ports. Red dots indicate where the laser line falls on test cards inserted at other ports.

in the test section as a reference, the centreline offset of the laser plane falling on additional cards inserted into ports in the channel (see Figure 3.1) allowed the radius of curvature to be computed. The results are shown in Table 3.2. The Dean number ($De \equiv 2(h/R_c)^{0.5}Re$) in the most curved section was 487, which indicates that the centripetal force was small compared to streamwise pressure gradient force (Berger *et al.*, 1983), and thus the curvature of the channel did not have an appreciable effect on the flow.

Table 3.2: Channel curvature measurements.

Ports	R_c (m)
2, 4, 6	145
4, 6, 7	84
6, 7, 8-1	59
7, 8-1, 8-2B	61

3.1.1.2 Velocity Field

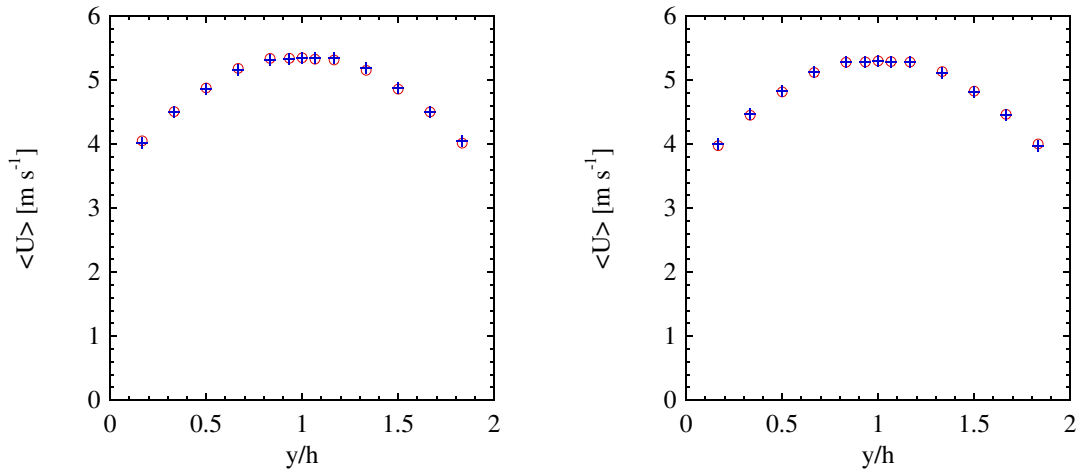
Once the physical dimensions of the channel had been verified, the velocity field in the test section was analysed. Streamwise (longitudinal) velocity measurements were taken at ports 8-1 and 8-2B using the hot-wire anemometry equipment described in Chapter 2, and the results are shown in Figures 3.2, 3.3, and 3.4.

Figure 3.2 (a) and (b) show the longitudinal mean velocity ($\langle U \rangle$) profiles at ports 8-1, and 8-2B, respectively. The data is also shown flipped about the centreline $y/h = 1$ to show the symmetry of the velocity field. Figure 3.2 (c) shows the two profiles plotted together which demonstrates the non-varying nature of the velocity field in the streamwise direction (the maximum difference is 1.8%). Overall, the maximum error with regards to symmetry is 0.9% at port 8-1, and 0.7% at port 8-2B.

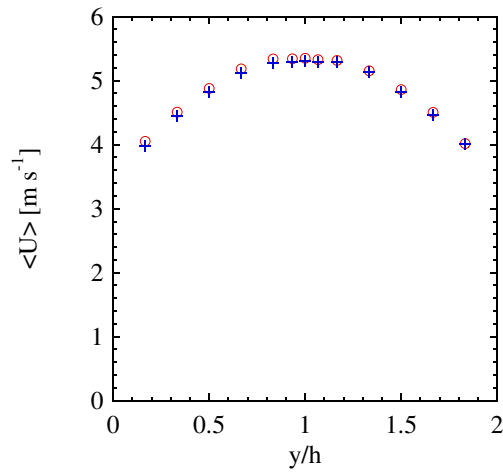
Root-mean-square (rms) longitudinal velocity fluctuations (u_{rms}) are similarly plotted in Figure 3.3, again at ports (a) 8-1 and (b) 8-2B. Part (c) shows good collapse of the two profiles, with a maximum error of 3.0% between the two ports. Here, the maximum error in symmetry is 4.9% and 2.2% for ports 8-1 and 8-2B, respectively.

Near-wall velocity measurements were also made using a specialized TSI 1218 probe. The near-wall longitudinal velocity profile, plotted non-dimensionally, is shown in Figure 3.4. Also plotted are i) the log-law inertial sublayer prediction $u^+ = 2.44 \ln(y^+) + 5.2$ (dashed line), and ii) the viscous sublayer prediction $u^+ = y^+$ (solid line). As discussed in Chapter 1, the velocities are non-dimensionalized by the friction velocity u_* such that $u^+ = \langle U \rangle / u_*$. The friction velocity is calculated (Tennekes & Lumley, 1972) from the (constant) pressure drop per unit length in the channel of 2.63 Pa m^{-1} measured by McLeod (2000) and confirmed by Lavertu (2002) and Costa-Patry (2005) under identical experimental conditions as the present work. Using Equation 3.1, u_* is found to be 0.256 m s^{-1} . The difference between the measured and predicted values of the velocity profile can be attributed to i) the $\pm 5\%$ variation of the quoted fit constants for the log law (see Chapter 1), ii) the difficulty of precisely determining the y -coordinate of the probe for near-wall measurements, and iii) the limited number of measurements in the viscous sublayer region.

$$u_* = \sqrt{\left| \frac{dP}{dx} \right| \frac{h}{\rho}} \quad (3.1)$$

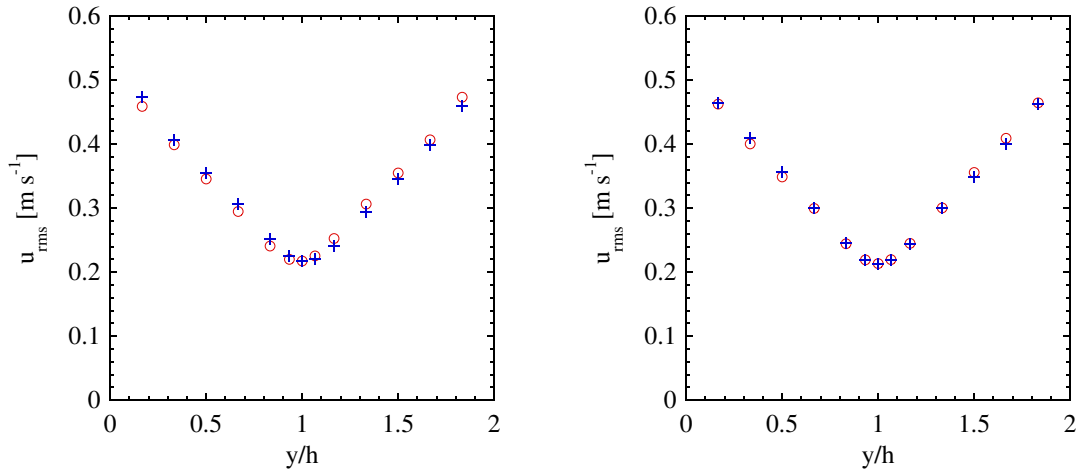


(a) Mean longitudinal velocity profiles at port 8-1. \circ : measured data, +: data flipped about $y/h = 1$. (b) Mean longitudinal velocity profiles at port 8-2B. \circ : measured data, +: data flipped about $y/h = 1$.

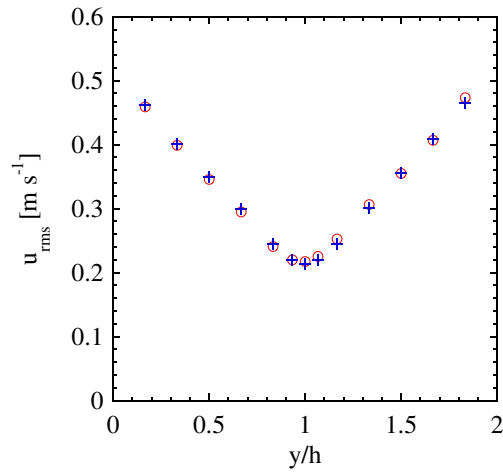


(c) Comparison of the mean longitudinal velocity profiles at two downstream locations. \circ : port 8-1, +: port 8-2B.

Figure 3.2: Mean longitudinal velocity $\langle U \rangle$ profiles showing channel symmetry and fully developed flow.



(a) Longitudinal rms velocity profiles at port 8-1. \circ : measured data, $+$: data flipped about $y/h = 1$.
 (b) Longitudinal rms velocity profiles at port 8-2B. \circ : measured data, $+$: data flipped about $y/h = 1$.



(c) Comparison of longitudinal rms velocity profiles at two downstream locations. \circ : port 8-1, $+$: port 8-2B.

Figure 3.3: RMS longitudinal velocity fluctuation u_{rms} profiles showing channel symmetry and fully developed flow.

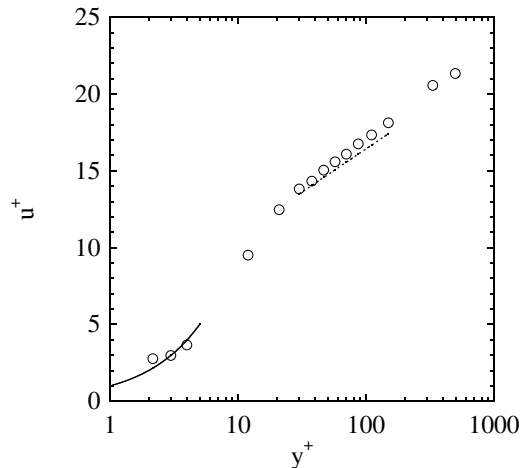


Figure 3.4: Near-wall non-dimensionalized longitudinal mean velocity profile; measured and predicted. \circ : measured, solid line: viscous sublayer prediction $u^+ = y^+$, dashed line: log-law inertial sublayer prediction $u^+ = 2.44 \ln(y^+) + 5.2$.

3.1.2 Passivity of the Scalar Field

By definition, a passive scalar has no dynamical effect on the fluid motion. It must be verified for the present work that the scalar (a small temperature excess) does not cause any buoyancy effects. If it did, it would alter the dynamics of the flow, as well as necessitating the addition of a buoyant production term ($g_j \langle \theta u_j \rangle / T$) to the TKE budget (Equation 1.7). By measuring the temperature-velocity correlation in the flow and comparing it to the dissipation rate of turbulent kinetic energy ϵ , Lavertu (2002) conservatively estimated the ratio of buoyant production to dissipation to be 1.7% for the identical flow. The scalar can thus be considered passive, and buoyancy effects negligible.

3.1.3 Source Obstruction Effects

It must also be confirmed that the presence of the line source does not appreciably impact the flow field. To test this, the Reynolds number over the line source is calculated as $Re_s = U_c d_s / \nu$, where d_s is the source diameter (0.127 mm and 0.254 mm for the small and large sources, respectively) and ν is the kinematic viscosity of the fluid. Evaluating at ambient conditions yields Re_s of 46 and 92. However, by taking into account the (higher) film temperature $T_{film} = \frac{1}{2}(T_s + T_\infty)$ around the line source (which increases viscosity and thus decreases the Reynolds number) the (hot) Re_s for the small and large line sources are 29 and 47, respectively. Although the critical Reynolds number for vortex shedding from a cylinder in crossflow (e.g., the line source) is 40 (Blevins, 1990), Lavertu (2002) showed that this is not a concern for the present work given that any small vortices shed by the source were masked by the (significantly larger) turbulent velocity fluctuations.

3.1.4 z-direction Invariance

McLeod (2000) showed experimentally that the velocity field is invariant in the z -direction in the region $z = \pm 0.275$ m. As all measurements in this work were taken in the test section at $z = 0$, it is assumed that the scalar field will also be invariant in the z -direction there.

3.1.5 Adiabatic Channel Walls

The channel walls are assumed to be adiabatic in the present work. Either a loss of heat to the surroundings, or an addition of external heat into the flow, would adversely affect the results. Lavertu & Mydlarski (2005) showed that the mean excess temperature is essentially zero when the line source is positioned at the centreline

($y_s/h = 1$). This indicated that there is no appreciable heat flux through the walls during the experiments, and the plume at $y_s/h = 1$ barely interacts with the channel walls at the x/h values under consideration.

3.2 Experimental Conditions

All experiments were conducted at (nominally) 21 °C, with typical variations of no more than ± 2 °C, and with an atmospheric pressure of nominally 101 kPa. The kinematic viscosity of air under these conditions is $1.53 \times 10^{-5} \text{ m s}^{-2}$. The blower speed was set to 432 rpm, yielding a centreline velocity $U_c = \langle U \rangle_{y/h=1} = 5.55 \text{ m s}^{-1}$. This results in a Reynolds number $Re \equiv \langle U \rangle_{y/h=1} h/\nu = 10,800$ since the channel half width h is 0.03 m.

In addition to the mean streamwise velocity $\langle U \rangle$ and rms longitudinal velocity fluctuation u_{rms} , three additional parameters are also useful to describe the velocity field. The first is the skewness of longitudinal velocity fluctuations, $S_u = \langle u^3 \rangle / \langle u^2 \rangle^{3/2}$, which is a measure of symmetry of the statistics. Second is the kurtosis $K_u = \langle u^4 \rangle / \langle u^2 \rangle^{4/2}$, which is a measure of the flatness of the probability density function (PDF) of the longitudinal velocity fluctuation (i.e., the likelihood of exceptionally large velocity fluctuations). Note that, for a Gaussian function, the skewness and kurtosis are 0 and 3, respectively. Lastly, the turbulent kinetic energy dissipation rate (ϵ) is an important parameter, in addition to being needed to calculate the Kolmogorov microscales of the flow.

Figure 3.5 presents profiles of (a) the skewness and (b) the kurtosis of the longitudinal velocity functions at port 8-2B. Positive skewness indicates that positive velocity functions are more probable. Conversely a negative skewness indicates that negative fluctuations occur more frequently. Near the wall, the skewness is positive since a large

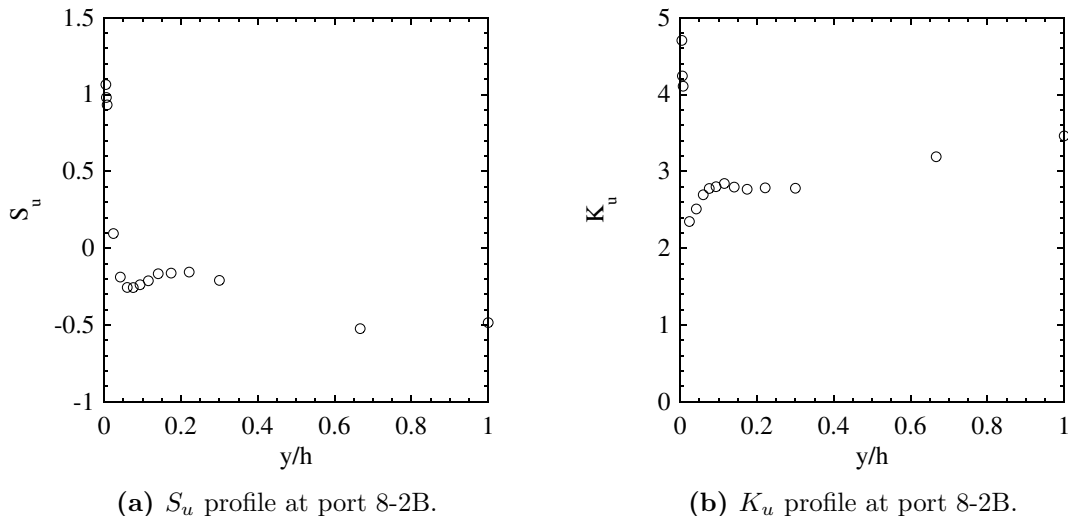


Figure 3.5: Profiles of the skewness (S_u) and kurtosis (K_u) of the longitudinal velocity fluctuations in the channel.

proportion of the velocity fluctuations are positive. This is because high-momentum fluid is predominantly transported *into* the near-wall region where the mean velocity is lowest. Analogously, at the centreline, the skewness is slightly negative because momentum transport from other parts of the flow creates more negative velocity fluctuations. In the near-wall region, the kurtosis is higher than 3 due to the large velocity gradients and subsequent production of turbulence in this region.

The TKE dissipation rate ($\epsilon = 2\nu \langle s_{ij}s_{ij} \rangle$) is used to compute a number of scales of the flow. It can also be determined from the dissipation spectrum $D(\kappa) = 2\nu\kappa^2 E(\kappa)$, where $E(\kappa)$ is the three-dimensional energy spectrum in the wavenumber κ . Following Tennekes & Lumley (1972):

$$\epsilon = 2\nu \langle s_{ij}s_{ij} \rangle = \int_0^\infty D(\kappa) d\kappa = 2\nu\kappa^2 \int_0^\infty E(\kappa) d\kappa . \quad (3.2)$$

Rewriting in terms of the one-dimensional longitudinal spectrum $E_{11}(\kappa_1)$ (which is

more readily measured), and assuming local isotropy:

$$\epsilon = 15\nu\kappa_1^2 \int_0^\infty E_{11}(\kappa_1) d\kappa . \quad (3.3)$$

By using Taylor's frozen flow hypothesis, which states that time t and downstream position x are related by an expression of the form $t = -x/\langle U_1 \rangle$ for flows wherein $u_{rms}/\langle U \rangle < 0.2$, the longitudinal wavenumber is related to frequency as $\kappa_1 = 2\pi f/\langle U_1 \rangle$.

As a result,

$$E_{11}(\kappa_1) = \frac{\langle U_1 \rangle}{2\pi} E_{11}(f), \text{ and} \quad (3.4)$$

$$\epsilon = \frac{60\nu\pi^2}{\langle U_1 \rangle^2} \int_0^\infty f^2 E_{11}(f) df . \quad (3.5)$$

Also, the integral length scale ℓ (which is the approximate size of the largest eddies) can be estimated (Tennekes & Lumley, 1972):

$$\ell \approx \frac{u_{rms}^3}{\epsilon} . \quad (3.6)$$

Finally, an intermediate length scale λ (called the Taylor microscale) can be determined from the relation (Tennekes & Lumley, 1972):

$$\left\langle \left(\frac{\partial u}{\partial x} \right)^2 \right\rangle \equiv \frac{\langle u^2 \rangle}{\lambda^2} = \frac{u_{rms}^2}{\lambda^2} . \quad (3.7)$$

For completeness, the turbulent Reynolds number, as well as those based on the integral and Taylor length scales (at the centreline) are given in Equations 3.8, 3.9, and 3.10, respectively.

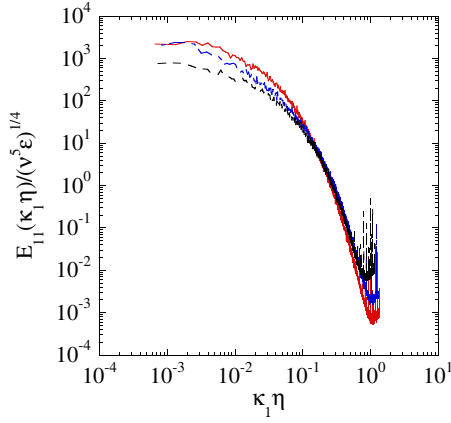


Figure 3.6: Non-dimensionalized spectra at 3 wall-normal locations. Red: $y/h = 0.024$, Blue: $y/h = 0.174$, Black: $y/h = 1.0$.

$$R_\tau \equiv \frac{u_* h}{\nu} = 502 \quad (3.8)$$

$$R_{\ell(y/h=1)} \equiv \frac{u_{rms(y/h=1)} \ell_{y/h=1}}{\nu} = 234 \quad (3.9)$$

$$R_{\lambda(y/h=1)} \equiv \frac{u_{rms(y/h=1)} \lambda_{y/h=1}}{\nu} = 58 \quad (3.10)$$

A summary of the discussed flow field properties and scales at three different wall-normal locations is given in Table 3.3. The one-dimensional energy spectra as a function of the longitudinal wavenumber are also presented in Figure 3.6.

Table 3.3: Summary of flow properties.

Parameter	Location		
	Buffer Layer	Inertial Sublayer	Centreline
y/h	0.024	0.174	1.000
y^+	12.0	87.5	502.
$\langle U \rangle$ (m s ⁻¹)	2.47	4.36	5.55
u_{rms} (m s ⁻¹)	0.695	0.473	0.222
S_u	0.095	-0.162	-0.485
K_u	2.35	2.77	3.46
ϵ (m ³ s ⁻²)	8.96	4.28	0.678
ℓ (mm)	37.6	24.7	16.1
λ (mm)	3.5	3.4	4.0
η (mm)	0.14	0.17	0.27
τ_ℓ (ms)	54.1	52.2	75.5
τ_η (ms)	1.31	1.89	4.75

Chapter 4

Results and Discussion

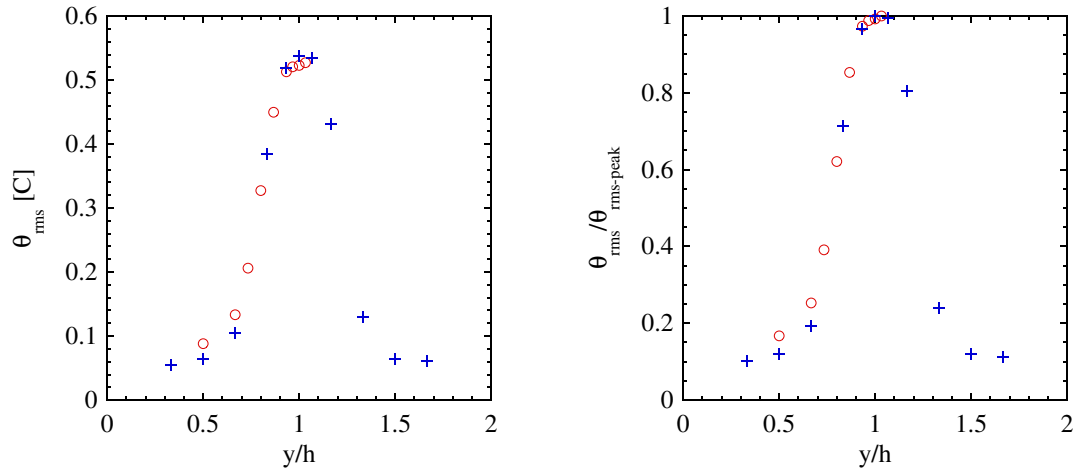
A discussion of the results of the present work is given in this chapter, which is divided into four sections. Section 4.1 presents the properties and downstream evolution of the scalar field in the channel, with comparisons to previous work. Results from the search algorithm development process are presented in Section 4.2. Section 4.3 details the one-dimensional search domain results. Since the maximum benefit of incorporating the physics of turbulent flows into the search algorithms is achieved in a two-dimensional search domain, a natural extension of the 1D work was made to examine the two-dimensional search case. This was achieved by modification of the experimental apparatus (discussed in Chapter 2), and source locating algorithms were developed and tested for the 2D search domain. A discussion of the search algorithms developed and the preliminary results from these tests are presented in Section 4.4.

4.1 The Scalar Field

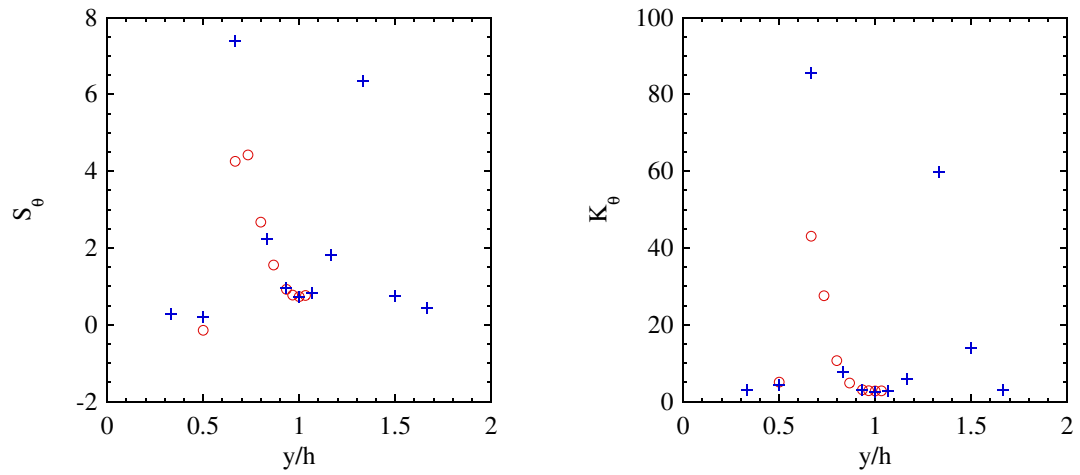
The passive scalar under consideration in the present work is a small temperature excess, measured using cold-wire thermometry (see Chapter 2). By means of a calibration (also discussed in Chapter 2), the output signal (voltage) of the CWT was converted to a raw total temperature, Θ . The total temperature Θ is a sum of the freestream temperature T_∞ , the mean temperature excess $\langle \Delta T \rangle$ (hereafter simply written as ΔT), and the temperature fluctuation θ , such that $\Theta = T_\infty + \Delta T + \theta$.

Initial measurements of the scalar field (emitted, in the present work, from a line source positioned at $y_s/h = 1$) were performed at a downstream position of $x/h = 4$ to verify the experimental setup prior to testing search algorithms. Tests were done at a Reynolds number of 10,800 and the line source input power set to 45 W m^{-1} . Filtered and unfiltered (see Chapter 2) data was recorded at 200 Hz, with 100 blocks (a group of samples, denoted as b) each of 4096 samples per block (spb) logged at each wall-normal position.

Figure 4.1 shows representative scalar statistics profiles taken during two different experiments (one full-width experiment using probe SN205-01 and one half-width experiment using probe SN205-02) of the (a) rms temperature fluctuation (θ_{rms}), (b) normalized temperature fluctuation ($\theta_{rms}/\theta_{rms-peak}$), (c) skewness of the temperature fluctuations (S_θ), and (d) kurtosis of the temperature fluctuations (K_θ). A small difference between the profiles can be seen for the higher-order statistics, which is a result of i) using two different probes (discussed below), and ii) slow convergence of high-order statistics on the edges of the plume, where the temperature field is intermittent. However, the results are similar to the (published and unpublished) data measured in the same channel by Lavertu (2002) and Costa-Patry (2005), as will be shown explicitly in Section 4.2 for a full range of downstream positions.



(a) RMS temperature fluctuation (θ_{rms}) profile. (b) Normalized temperature fluctuation ($\theta_{rms}/\theta_{rms-peak}$) profile.



(c) Profile of the skewness of temperature fluctuations (S_θ). (d) Profile of the kurtosis of temperature fluctuations (K_θ).

Figure 4.1: Example temperature fluctuation statistics profiles at Port 8-1, showing data taken during two experiments. \circ : half-width experiment (March 7, 2012), $+$: full-width experiment (January 23, 2012).

4.1.1 Sources of Error

Small differences of up to 20% between the results of the two different experiments can be seen in Figure 4.1 (a) and (b). There are a number of potential reasons for this, summarized briefly below. The comments apply equally to all measurements made for the present work. It should also be noted that small errors in magnitudes of the measured parameters do not appreciably affect the search results, since the searcher looks for the maxima (or, minima) of the search parameter, rather than a specific value.

4.1.1.1 Positioning Error

The true position of the searcher (probe) relative to the line source can have an error resulting from i) uncertainty in the exact y_s position (± 0.15 mm), ii) uncertainty in the wall-normal reference position (± 0.20 mm) since the probe has a finite width, and iii) uncertainty in the exact position of the traversing mechanism (± 0.005 mm). This results in a total positional uncertainty of ± 0.355 mm, or 1.2% of the channel half-width h . Considering as an example the effect on θ_{rms} , this causes an uncertainty of ± 0.018 °C since the maximal slope of $\partial\theta_{rms}/\partial y$ is 0.05 °C mm⁻¹.

In addition, for 2D searches, the positional uncertainty is increased because the movement plane is not perfectly aligned with the channel, and the range of motion is much larger. This results in a positional uncertainty of approximately ± 0.5 mm for both the x - and y -coordinates (1.7% of h). The positioning error does not directly affect the measured results (e.g., θ_{rms}), but does however introduce error into the 2D plume model, since it is based on both the measured parameter *and* the position of the searcher.

4.1.1.2 Cold-Wire Probe Differences

Since the cold-wire probes are extremely fragile and prone to breaking, different experiment sets were generally performed with different CW probes. As a result, calibration and equipment setup differences for the probes likely resulted in some error. Furthermore, the CW probes had to be removed from the channel and cleaned frequently in iso-propyl alcohol to remove contamination, which again caused slight differences in the measurements. The frequency response in particular was affected by contamination of the probes as detailed in Table 4.1 for probe SN203-05.

Table 4.1: Probe SN205-03 frequency response at different conditions.

Condition	Cut-off Frequency f_c (Hz)
pre-calibration	3150
post-calibration (contaminated)	2300
post-cleaning	3250

4.1.1.3 Reduced Statistical Convergence in the Edges of the Plume

The largest error arises from unconverged results for the extremely intermittent region in the edges of the plume. Although difficult to quantify, this is supported by the good agreement of the data in Figure 4.1 at the centre of the plume. Sampling larger data sets would serve to eliminate this error, but opposes a primary objective of this work which is to develop source locating algorithms that are fast and efficient.

4.1.1.4 Other Sources of Error

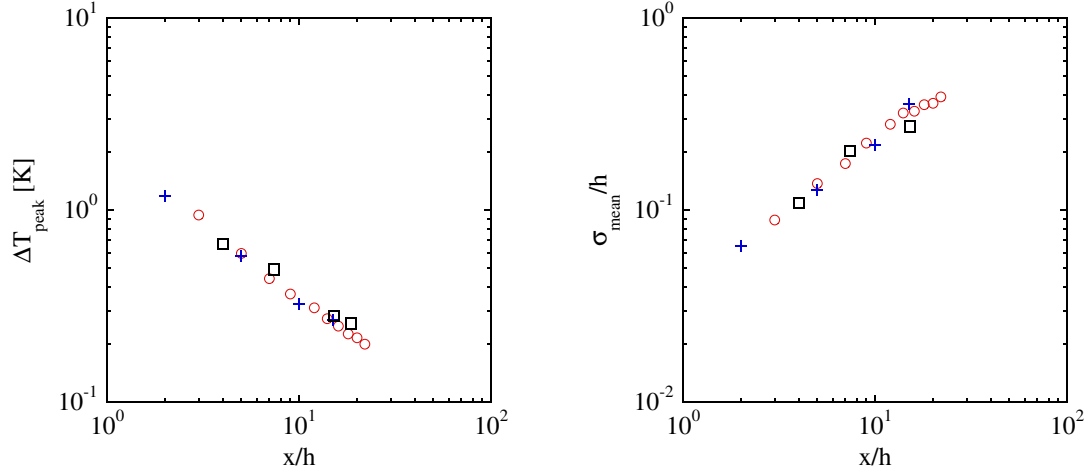
There is also a slight error introduced when the analogue voltage signal is quantized by the data acquisition card. The DAQ card has 16-bit resolution, so with a signal of ± 5 V the quantization error was ± 0.15 mV; however, the manufacturer-listed error at this signal level is ± 1.790 mV (approximately ± 0.005 °C for most experiments).

Finally, it should be noted that the channel is located in the McGill Aerodynamics Laboratory which also houses two other wind tunnels. Significant noise in the temperature data was noticed when the other wind tunnels were in operation, due to the modified airflow characteristics of the laboratory which affected both the intake conditions to the blower and freestream room temperature T_∞ . Thus all final experiments were performed when the other wind tunnels were not operating.

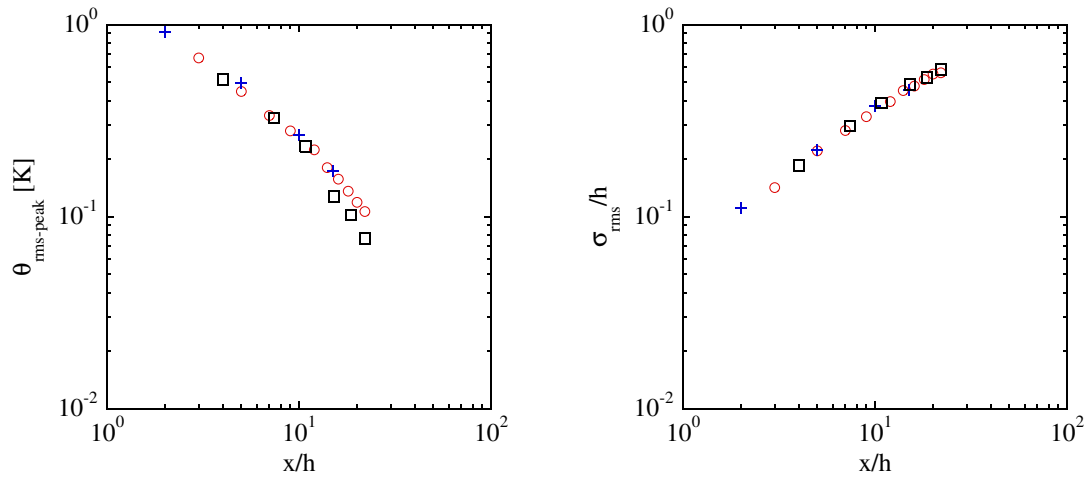
4.1.2 Downstream Evolution

Of particular interest to the present work is the downstream evolution of the scalar field. To this end, Figure 4.2 shows a comparison of the evolution of the (a) peak mean temperature excess (ΔT_{peak}), (b) standard deviation (i.e., width) of the mean temperature excess profile, non-dimensionalized by the channel half width (σ_{mean}/h), (c) peak rms temperature fluctuation ($\theta_{rms-peak}$), and (d) standard deviation of the rms temperature fluctuation profile, again non-dimensionalized by the channel half width (σ_{rms}/h). The data from the present work is plotted along with results from Lavertu & Mydlarski (2005), and Germaine (2011; unpublished) for the range $2 \leq x/h \leq 22$. Very good agreement can be seen between the three data sets, for a large range of downstream positions. The exact nature of the downstream evolution of the statistics will be discussed in Section 4.4.1, where the plume model is developed.

Note that the standard deviation of the profile of a parameter (e.g., mean temperature excess, or rms temperature fluctuation) will often be given when discussing the results. It is one of two convenient ways of quantifying the width of a Gaussian-like profile; the half-width at half-maximum (HWHM) (or $z_{1/2}$) being the other. For an arbitrary parameter p , the two are related as $z_{1/2}^p = \sqrt{2 \ln 2} \sigma_p \approx 1.177 \sigma_p$, assuming a Gaussian distribution.



(a) Downstream evolution of peak mean temperature excess (ΔT_{peak}). (b) Downstream evolution of the standard deviation of the mean temperature excess (σ_{mean}) profile, non-dimensionalized by the channel half-width h .



(c) Downstream evolution of peak rms temperature fluctuation ($\theta_{rms-peak}$). (d) Downstream evolution of the width of the rms temperature fluctuation profile (σ_{rms}), non-dimensionalized by the channel half-width h .

Figure 4.2: Comparison of the downstream evolution of the scalar field to previous laboratory work. \circ : present work, $+$: E. Germaine (2011), \square : R. Lavertu (2002).

4.2 Algorithm Development

4.2.1 Search Parameters

Both singular statistics and compound parameters were studied as primary search parameters in the present work, as listed below. They all increase towards a maxima (or, conversely, decrease towards a minima) within the plume boundaries.

1. Singular statistics:

- (a) ΔT , the mean temperature excess
- (b) θ_{rms} , the rms temperature fluctuation
- (c) S_θ , the skewness of the temperature fluctuations
- (d) K_θ , the kurtosis of the temperature fluctuations

2. Compound parameters:

- (a) $\theta_{rms}/\Delta T$, rms-to-mean ratio (a surrogate for the peak-to-mean ratio)
- (b) S_θ/θ_{rms} , skewness-to-rms ratio
- (c) $\Delta T/(S_\theta/\theta_{rms})$, which combines three singular parameters

Searches with K_θ as the primary search parameter were (quickly) ruled out as the convergence was (expectedly) much slower (see Section 4.2.2).

The skewness-to-rms ratio S_θ/θ_{rms} was proposed as a search parameter because of its behaviour towards the source of the scalar plume. θ_{rms} increases from 0 (not accounting for background noise) to a peak at the source location, while S_θ decreases from a peak at the edge of the plume to a (local) minimum at the source location. The ratio S_θ/θ_{rms} amplifies these two simultaneous trends resulting in an quickly-decreasing function towards the source location. Likewise, the ratio $\Delta T/(S_\theta/\theta_{rms})$ aimed to incorporate all the better noise-resistant qualities of using ΔT into the search for minimum S_θ/θ_{rms} .

Noting that the freestream temperature T_∞ is not important to the searcher, it can be removed from the data through one of two methods: i) by high-pass filtering the signal (however, this also removes the mean temperature excess ΔT), or ii) by gathering a reference temperature prior to every experiment/search. The second method was used in most of the experiments, once it was determined that the ΔT data was highly useful in the search algorithms. To do this, at the beginning of every search run, the searcher (probe) moved to a location far outside of the plume (known *a priori*) to determine the freestream temperature. This value was then subtracted from all subsequent raw temperature measurements, both inside and outside of the plume. It also allowed the long-term freestream temperature to be tracked to partially determine the effect of the other wind tunnels being activated in the preliminary experiments.

4.2.2 Convergence Analysis

As one of the primary goals of the present work is developing efficient search algorithms, a study was performed to determine the rate of convergence of the statistics for different search parameters. This allowed the tradeoff between measurement time and measurement accuracy to be determined, alluded to earlier with respect to the higher-order statistics.

Typical plots (with the probe positioned at $x/h = 4$, $y/h = 1$) of the converging statistics of the i) mean temperature excess (ΔT), ii) rms temperature fluctuation (θ_{rms}), iii) skewness of the temperature fluctuations (S_θ), and iv) kurtosis of the temperature fluctuations (K_θ) are shown in Figure 4.3. The measurements in this case was again conducted at $Re = 10,800$, a line source input power of 45 W m^{-1} , and the data was recorded at 200 Hz, with 800 blocks (b) each of 256 samples per block (spb) logged at each wall-normal position.

To create the plot, the final converged value of the parameter is calculated by analysing

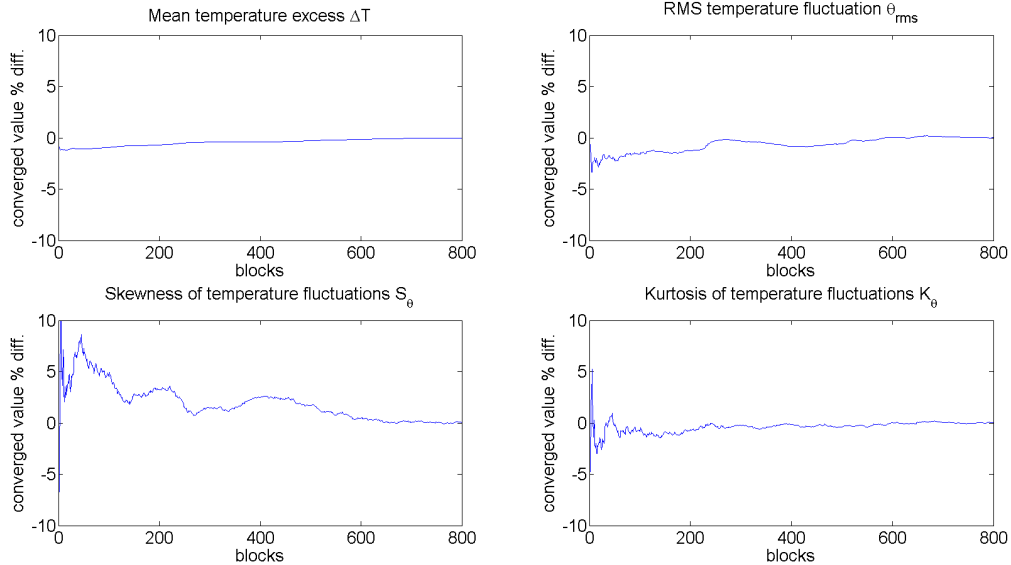


Figure 4.3: Convergence of the temperature statistics at the channel centreline.

the entire data set (all 800 blocks). Then, the percent difference between the 0 – n th block statistic (e.g., the statistic calculated for blocks 0 – 5) and the final converged value is determined for all data blocks sets. Traces of these percent differences are shown in Figure 4.3. As can be seen, the mean temperature excess and rms temperature fluctuation converge very quickly, while the higher-order statistics (S_θ and K_θ) take much longer to converge. For example, after only 1 b (~ 1.3 s sampling time), ΔT stays within 1% of its final converged value. θ_{rms} takes approximately 100 b (~ 2 min) to reach this level of convergence. However, (S_θ and K_θ) often took more than 400 b (~ 9 min) to stay within these limits (noting that, for the particular data set shown in Figure 4.3, K_θ converges more quickly than S_θ in about 300 b).

Figure 4.4 shows the number of data blocks required for convergence of (a) ΔT , (b) θ_{rms} , and (c) S_θ versus the relative wall-normal distance from the source, non-dimensionalized by the mean temperature excess profile standard deviation (σ_{mean}). All data was recorded at 200 Hz, and 256 spb. Since S_θ in particular converges so slowly, the convergence thresholds are set to 1% for ΔT , 2% for θ_{rms} , and 5% for S_θ . In addition to calculating the number of blocks at which the statistics were fully

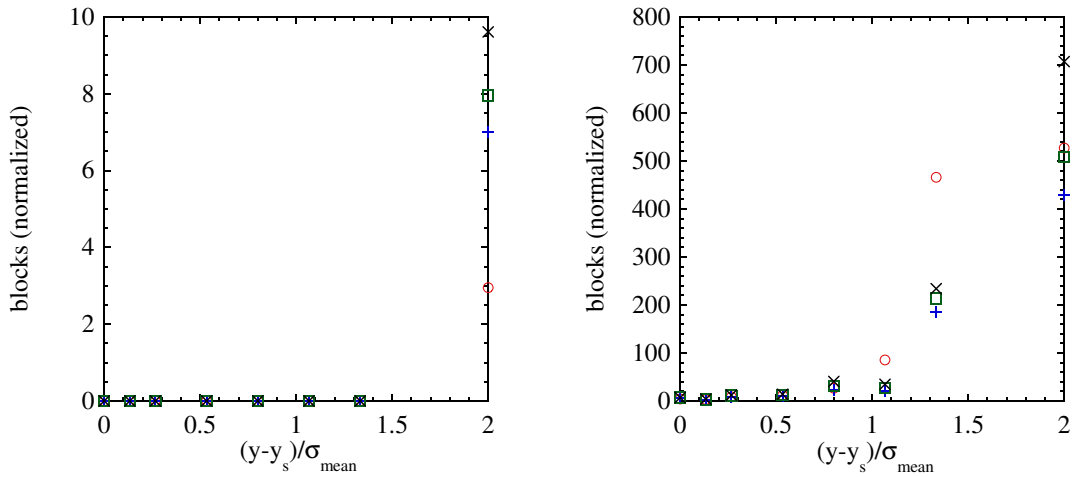
(continuously) converged, the other symbols denote the time it takes to reach the percent difference and stay at that level for at least i) 5, ii) 10, and iii) 20 consecutive blocks. While varying speeds of convergence are shown (with higher-order statistics converging more slowly, as expected), it is noted that convergence is much quicker for all statistics measured within the plume.

4.2.3 Starting Position

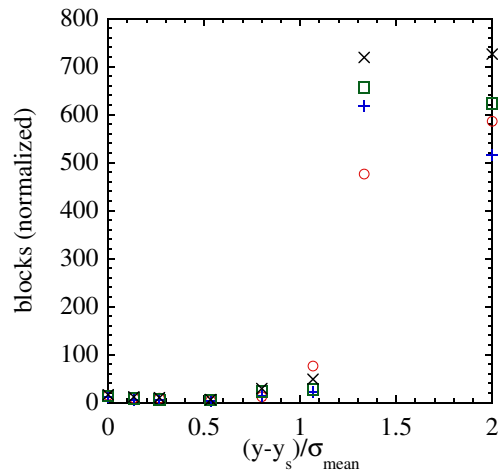
The starting position of the searcher was chosen from a uniform random distribution bounded by the physical dimensions of the channel in the 1D search case (i.e., $y = 0 - 60$ mm). In the 2D case, the same uniform distribution was used for the y -coordinate, and a set of fixed downstream starting positions was used. Batches of searches were started at $x = 150, 210, 270, 330,$ and 390 mm ($x/h = 5, 7, 9, 11,$ and 13). Since the search algorithm needed to remain agnostic towards the search domain, approximately 30% of all searches were terminated when the algorithm requested positions exceeding the physical bounds of the channel.

4.2.4 Binary Plume Threshold

At the beginning of every test, the searcher must determine whether it is inside or outside of the scalar plume. In keeping with the majority of the literature (e.g., Lo Iacono (2010)), a binary concentration cut-off was used. This is also in accordance with the fact that the sampling rate of 200 Hz does not capture the fine-scale structure of the scalar field. A mean temperature excess threshold of four times the background noise was found to be optimal. This meant that the searcher was declared to be in the plume when $\Delta T > 4\sigma_{background-noise}$. The background noise was found (as discussed in Chapter 2) by moving to an *a priori* known location far outside the plume and taking



(a) Convergence of the mean temperature excess (ΔT). (b) Convergence of the temperature fluctuation (θ_{rms}).



(c) Convergence of the skewness of temperature fluctuations (S_θ).

Figure 4.4: Comparison of the number of data blocks required for convergence of the scalar statistics, vs. wall-normal position non-dimensionalized by the mean temperature excess profile standard deviation (σ_{mean}). Symbols represent convergence for \circ : continuous, $+$: 5 blocks, \square : 10 blocks, \times : 20 blocks.

and processing a reference measurement there. Typical values of σ_{b-n} were around 0.03 – 0.035 K, yielding a cut-off for ΔT in the range 0.12 – 0.14 K. When the other wind tunnels in the laboratory were operating, σ_{b-n} increased approximately 15% to 0.035 – 0.04 K.

4.2.5 Plume Finding/Explorative Phase

When the searcher starts outside of the plume, it must enter an explorative search phase. A bio-mimetic, expanding ‘zig-zag’ mode was used for all experiments in the present work. Its underlying principle is that when there is a lack of information, moving to a new location is almost always preferable to staying on station. This method has been used in robotic experiments (e.g., Lochmatter *et al.* (2008)), and also noted in animal behaviour (e.g., Mafra-Neto & Carde (1994)). Different levels of zig-zag expansion were tested; a 2 – 3 mm (0.067 – 0.1*h*) step size was found to appropriately balance the competing interests of quickly searching the entire domain and yet not missing the plume altogether. After a number of measurements, the searcher would either find the plume and move to the exploitive phase, or request to move outside of the physical domain, in which case the run was terminated.

4.2.6 Plume Traversal/Exploitive Phase

Once the searcher had found the plume, the next step was to use data from measurements within the plume to locate the source. Simple methods (such as a linear gradient climb) were found to be slightly slower, but much more robust than more complex extrapolative/predictive methods (such as parabolic extrapolation). The most studied exploitive phase in this work was a linear gradient climb (or descent). Once inside the plume, the searcher would step either up (for a maximum, e.g., ΔT)

or down (for a minimum, e.g., S_θ) the gradient of the primary search parameter. The source was declared once the maximum/minimum had been passed (i.e., when the gradient was found to have switched directions).

A perfect search algorithm under these conditions would declare the source to be at $y'_s = 30$ mm ($\pm \frac{1}{2} \times$ step size), with a (minimum) standard deviation of the profile of declared source locations (ς_{y_s}) that depends on the step size used. Since a larger step size decreases the maximum achievable accuracy, but at the same time reduces the search time (since less measurements are taken), a balance between the two competing interests must be found. A step size of 1 mm was used in the present work to provide such a balance. The standard deviation of a uniform distribution on $[29.5, 30.5]$ mm can easily be calculated, yielding the best-case $\varsigma_{y_s} = 0.29$ mm.

4.2.7 Algorithm Template

The overall algorithm template typical of the type developed for the present work is summarized below in five steps:

1. Position the traversing mechanism
 - (a) Beginning of a search: random start position
 - (b) Continuation of a search: calculated position
2. Acquire and record raw $\tilde{\Theta}$ -data
3. Analyse the current data
4. Analyse the aggregate data
5. Declare source?
 - (a) No: determine next data point and return to step 1 (b), or terminate
 - (b) Yes: search is complete

Step 1 varies based on whether it is the first measurement of the search or not. Step 5 determines whether to declare the source (in which case the search ends) or to continue searching and return to step 1. Algorithms based on these steps were developed for both the one-dimensional and two-dimensional search regimes.

It should be noted that the original experimental apparatus was limited to a 1D search domain. All of the results from the previously described algorithm development process were thus incorporated into a 1D search algorithm and tested in the channel (discussed in Section 4.3). Turbulence physics is not directly applicable to the 1D search case, other than to help understand the physical interpretation and expected trends of the search parameters. As such, after the core search algorithm was developed and tested in the 1D case, the work was extended to a 2D search domain (discussed in Section 4.4) where a knowledge of turbulence physics was more useful.

4.3 One-Dimensional Search Domain Results

An easily customizable search algorithm was devised and implemented in MATLAB that enabled a wide range of search and measurement parameters to be tested. The strategy was a two-phase (plume finding and plume traversal, using distinct processes for each) hybrid line search (which combines the concepts of zig-zagging and gradient climb) with ambient background compensation (which determines and compensates for the background conditions at the beginning of each run).

The searcher (a CW probe mounted on a traversing mechanism) first moves to an *a priori* known location far from the scalar plume. Data is recorded to determine the ambient background statistics of the mean temperature and rms temperature fluctuation. This allows the removal of T_∞ from the raw data, as well as the scalar

concentration cut-off ($4\sigma_{b-n}$) to be determined. The searcher then proceeds to a random location within the search domain bounds. The initial plume finding phase uses a zig-zagging approach, to search for the plume (which is found when the mean temperature excess exceeds the determined threshold), at which point it switches to the second phase. The expansion of the search zone is linear and adjustable, along with all values related to the search parameter and measuring details (e.g., sample time). The second phase of the search is exploitive and performs a gradient climb based on the primary search parameter, which again is configurable along with all other measuring details and chosen based on a knowledge of turbulent scalar plumes to provide good characteristics (e.g., a profile with a sharp gradient) for the searcher. The source is declared once the gradient climb is complete, and data such as final parameter value, total search time, total movement distance, etc. is recorded.

Figures 4.5, 4.6, 4.7, and 4.8 show representative data from four different experiments, each with 100 searches. Any searches that were terminated due to the algorithm requesting a move outside of the domain boundaries are removed from the data. Traces of the i) measured parameter vs. measurement number, ii) aggregate parameter profile, iii) searcher position vs. measurement number, and iv) a histogram of the declared source location are all shown. The results are also tabulated in Table 4.2.

The value of the search parameter as recorded by the searcher at all points during a run is traced by each line. The starting value is entirely dependent on the (random) starting position, and the gradient climb technique can be clearly seen towards the end of each trace, as can the drop for the last measurement where the peak has been passed. An aggregate profile of every recorded position-parameter value pair is shown in each figure, providing a sense for the overall or true parameter profile. Slight scatter in the data results from the extremely short total sample times used in the algorithm (discussed later). Also shown is a trace of the searcher's position

at each point of measurement, which clearly shows the two phases (zig-zagging and gradient climb) of the search algorithm. Lastly, a histogram of the declared source positions is given.

Average total search time is a function of the number of measurements made and the time per measurement, which in turn is a function of the total number of blocks recorded and samples per block. The first three sample search summaries have approximately equal average search times, as the average number of data points is similar and the data recording parameters are identical. As can be seen, using $\theta_{rms}/\Delta T$ as the primary parameter yields the most accurate results (lowest ς_{ys}). Furthermore, reducing the sample time by a factor of 4 for the $\theta_{rms}/\Delta T$ searches still results in good accuracy compared to searches for peak θ_{rms} . Graphical summaries of searches for the other four primary search parameters (S_θ , K_θ , S_θ/θ_{rms} , and $\Delta T/(S_\theta/\theta_{rms})$) are not provided for brevity, but exhibit similar trends with respect to accuracy vs. search time. The results are however shown in Figure 4.9, discussed below.

It is interesting to note that both mean temperature excess and rms temperature fluctuation profiles increase monotonically towards the source from outside of the plume bounds. However, the rms-to-mean ratio decreases towards the source, but only inside of the plume; outside of the plume, its value can vary widely. At the edge of the plume, the ratio can reach very high magnitudes (negative values are non-physical and a result of ΔT being measured very slightly below 0 (e.g., -0.01 K) due to noise) and so the graphs are clipped. Thus, for this search parameter, the binary plume cut-off prevents the algorithm from using non-useful parameter data from outside the plume. Furthermore, the rms-to-mean parameter ratio $\theta_{rms}/\Delta T$ can be viewed as a surrogate for a peak-to-mean ratio. It has been postulated (Baker *et al.*, 1998; Lo Iacono, 2010) that insects and other biological organisms are in fact more sensitive to the peak-to-mean ratio of the scalar than either the peak or average

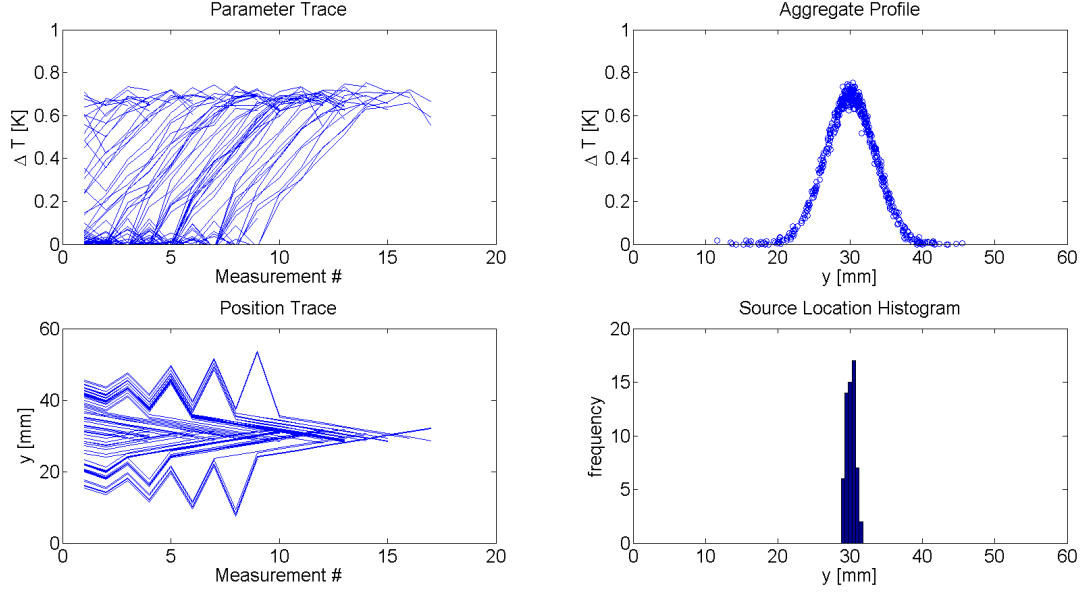


Figure 4.5: Search results for mean temperature excess (ΔT). Each measurement is 2 blocks long with 256 samples per block.

Table 4.2: Summary of 1D search results (shown in Figures 4.5, 4.6, 4.7, and 4.8) for different parameters and sample times.

Search Parameter	Samples	Blocks	y'_s (mm)	ζ_{ys} (mm)
ΔT	256	2	30.1	0.64
θ_{rms}	256	2	29.9	1.78
$\theta_{rms}/\Delta T$	256	2	30.0	0.59
$\theta_{rms}/\Delta T$	128	1	30.0	1.32

concentration individually.

Figure 4.9 shows the results for all search parameters tested, as well as the effect of higher background noise (when the other wind tunnels in the laboratory were operating). For all points, the ordinate is the width (standard deviation) of the declared source location profile (ζ_{ys}), non-dimensionalized by the channel half-width h , which is a measure of the accuracy of the algorithm. The abscissa of each point is the number of blocks (at 256 spb) of data recorded and analysed at each measurement location. Results are shown for five of the primary search parameters. (The others, S_θ and K_θ were only tested once due to poor performance resulting from the partic-

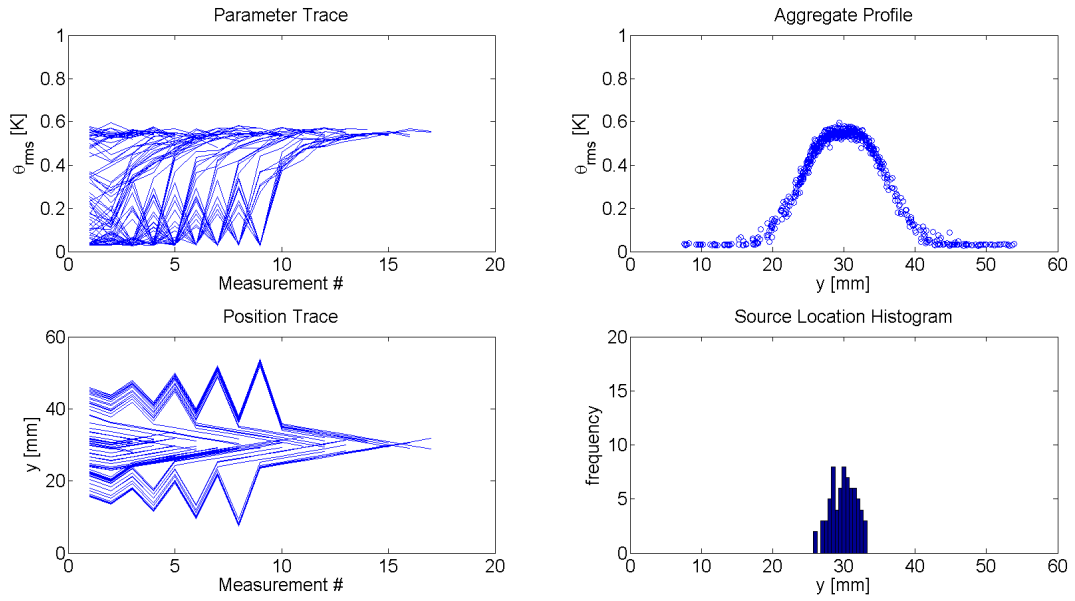


Figure 4.6: Search results for rms temperature fluctuation (θ_{rms}). Each measurement is 2 blocks long with 256 samples per block.

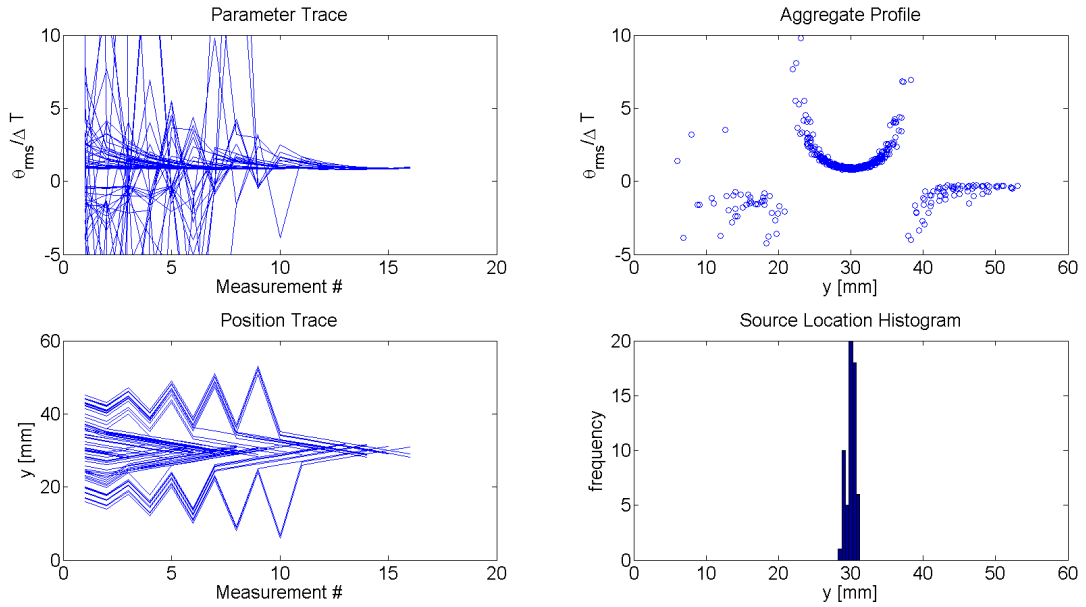


Figure 4.7: Search results for rms-to-mean ratio ($\theta_{rms}/\Delta T$). Each measurement is 2 blocks long with 256 samples per block.

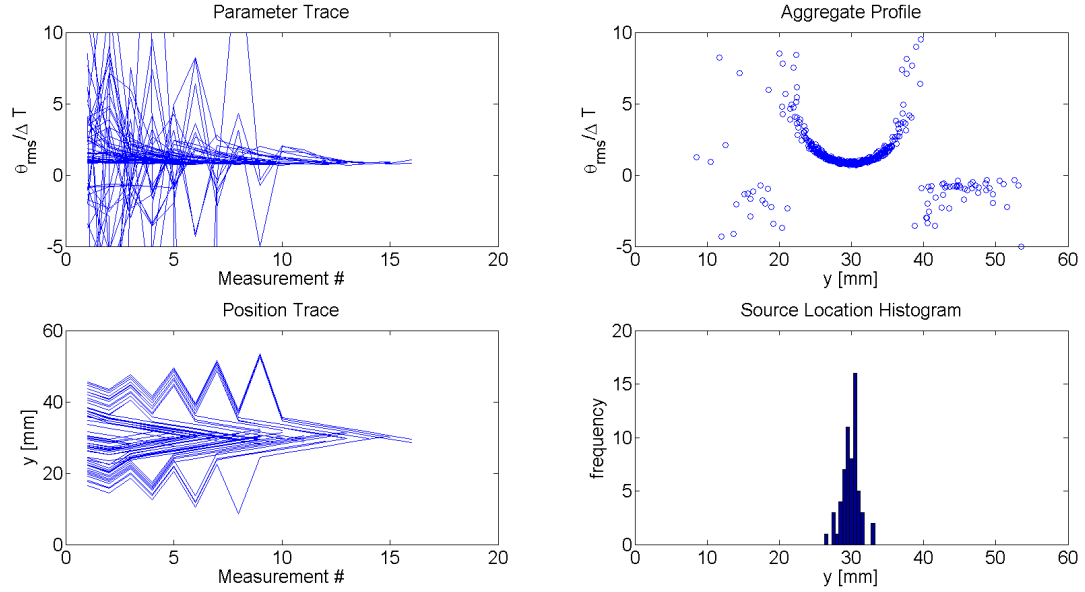


Figure 4.8: Search results for rms-to-mean ratio ($\theta_{rms}/\Delta T$). Each measurement is 1 block long with 128 samples per block.

ularly long convergence times.) The points are curve-fit with a decaying exponential function to approximate the ‘diminishing returns’ effect of taking more total samples per measurement. Lastly, note that the filled symbols and solid lines indicate experiments conducted with the other wind tunnels off; open symbols and dashed lines are for experiments done with the other wind tunnel operating.

The tradeoff between speed and accuracy can be seen clearly in the figure. That is, taking more samples (blocks) for each measurement results in a longer total search time, but a more accurate result (lower ζ_{ys}/h). However, an incremental increase in accuracy requires higher and higher search times to achieve. Higher-order statistics (e.g., S_θ ; not shown) provide more accurate results, but are only reliable when data is averaged over a longer time (higher number of blocks). Simpler search parameters such as the mean temperature excess (ΔT) show increased accuracy, even with very short averaging times, but were more affected and exhibited a large decrease in accuracy when noise was present. More complex mixed search parameters (e.g., S_θ/θ_{rms}) showed better resilience to noise. The best overall results (in terms of speed

and accuracy, as well as robustness towards noise) are provided by using $\theta_{rms}/\Delta T$ as the primary search parameter. This is a particularly interesting result since, as mentioned previously, it has been postulated that insects and other biological organisms are more sensitive to the peak-to-mean ratio of the scalar than either the peak or average concentration individually.

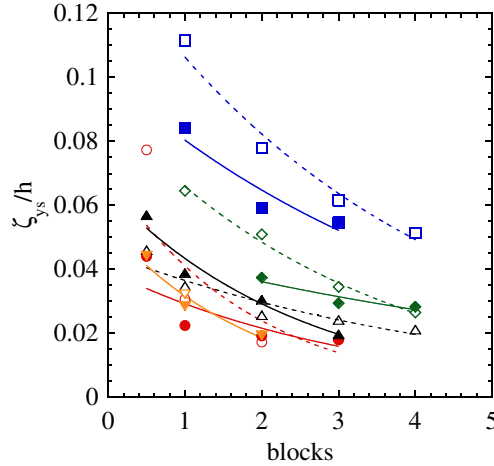


Figure 4.9: Accuracy vs. search time tradeoff for different search parameters. Open symbols, dashed lines: big tunnel on; filled symbols, solid lines: big tunnel off. \circ : ΔT , \square : θ_{rms} , \diamond : S_{θ}/θ_{rms} , \triangle : $\Delta T/(S_{\theta}/\theta_{rms})$, ∇ : $\theta_{rms}/\Delta T$.

4.4 Two-Dimensional Search Domain Results

Since the original experimental setup was limited to a one-dimensional search domain, the algorithms were not able to reduce the search domain entropy with every measurement step. That is, it was not possible to determine (for every measurement) that the source was *not* at the present location. As such, the total amount of information gain for the searcher at each step was limited and varied. Also, a knowledge of the turbulent scalar plume and the flow that advects it is better able to be used in the two-dimensional search case since behaviour in its downstream evolution could

not be incorporated into the algorithm. Given that the possible search parameters had been evaluated in the 1D problem, the work can now be extended to a 2D search domain.

In the 2D searches, the starting y -position was chosen in the same manner as the 1D search experiments, and the same concentration cut-off threshold was used. Searches were performed starting at five different downstream locations as noted in Section 4.2.3. To properly incorporate the physics of turbulent flows into the 2D search algorithms, a model of the scalar plume was first developed.

4.4.1 Scalar Field Model

By using a model of the scalar plume, the searcher can follow an *infotaxis*-based approach in searching for the source location. The primary idea behind an *infotactic* search is that the searcher should choose the next measurement location that will maximize the expected rate of information gain (i.e., reduce the entropy) (Vergassola *et al.*, 2007). A suitable plume model, updated with each measurement, provides a mechanism for this.

The peak mean temperature excess (ΔT_{peak}) and peak rms scalar fluctuation ($\theta_{rms-peak}$) both decay in the streamwise direction following approximate power laws (e.g., $\sim x^{-n}$) (Warhaft, 1984; Lavertu & Mydlarski, 2005). This power-law decay can be (roughly) extended to the off-axis mean temperature excess (ΔT) and rms temperature fluctuation (θ_{rms}). In addition, the profile half-widths (σ_{mean} and σ_{rms} , respectively) also approximately follow a power law behaviour ($\sim x^{+m}$). At least two points are required to fit the data to a general power-law curve Ax^n . Based on measurements from the present work, as well as those from Lavertu (2002), Costa-Patry (2005), and Germaine (2011; unpublished), the approximate exponents on x are -0.6 , $+0.7$, -0.9 and $+0.7$ for ΔT , σ_{mean} , θ_{rms} and σ_{θ} , respectively. Thus, as an example and for a

fixed wall-normal position $y = C$, the mean temperature excess can be approximated by $\Delta T(x, y = C) \simeq Ax^n$ where $n \approx -0.6$ and A is a constant to be determined.

The standard form of a Gaussian function is (for real constants a, b, c):

$$f(y) = ae^{-\frac{(y-b)^2}{2c^2}} . \quad (4.1)$$

This is more normally written as:

$$f(y) = A \exp \left\{ -\frac{(y - \mu)^2}{2\sigma^2} \right\} , \quad (4.2)$$

where A is the peak value of the function (at $y = \mu$), μ is the centre of function, and σ is the standard deviation which as previously noted is a measure of the profile width. Thus, for a fixed downstream position $x = C$,

$$f(x = C, y) = AC^n \exp \left\{ -\frac{(y - y'_s)^2}{2[\sigma(C)]^2} \right\} , \quad (4.3)$$

where f can be either ΔT or θ_{rms} . Since the distribution width also grows according to an approximate power law $\sim x^m$, where $m \approx +0.7$, and $\sigma(C) \simeq Bx^m$, the two-dimensional scalar field has the approximate (5-parameter) form:

$$f(x, y) = Ax^n \exp \left\{ -\frac{(y - y'_s)^2}{2B^2x^{2m}} \right\} , \quad (4.4)$$

where A is again a measure of the peak magnitude (at the source location y'_s) of ΔT or θ_{rms} , n is power-law exponent for the peak (decay), y'_s is the predicted source location, B is a measure of the maximum profile width, and m is the profile width power-law (growth) exponent. Figure 4.10 shows a representative plot of mean temperature excess data fit to the 5-parameter plume model in (a) isometric, and (b) planar view.

As per the model, the data is fit to Gaussian function in the wall-normal direction and a power law in the streamwise axis. The trending of this particular parameter towards 0 outside of the plume can be seen, along with the sharp peak close to the source position upstream. Also visible is the slow widening (and corresponding decrease in magnitude, since the total thermal energy contained in the plume remains constant) of the plume as it evolves downstream. Of course, in the present flow, it can never become larger than the defining geometry.

4.4.2 Sample Search

After zig-zagging and acquiring at least three data points inside the plume at the starting downstream position, the searcher is able to generate a 1D model of the scalar plume. An upwind advancement of 30 mm ($\Delta x/h = -1$) is performed and two further measurements are taken at the pre-computed inflection points of the Gaussian profile. With 5 data points, the full 2D 5-parameter scalar plume model can now be fit yielding values for A , n , y'_s , B and m . The searcher then continues advancing upwind, taking either one (alternating sides of y'_s), or two more measurements per downstream position, and continuously refines the surface fit. An example series of successive scalar model fits to mean temperature excess data is shown in Figure 4.11. It can be seen that as more data points are collected, the fit becomes much better defined and more accurately matches the true parameter values for all locations in the plume. Data is only shown starting from $x/h = 1$ because the non-physical nature of the model farther upstream causes the magnitude to be very large.

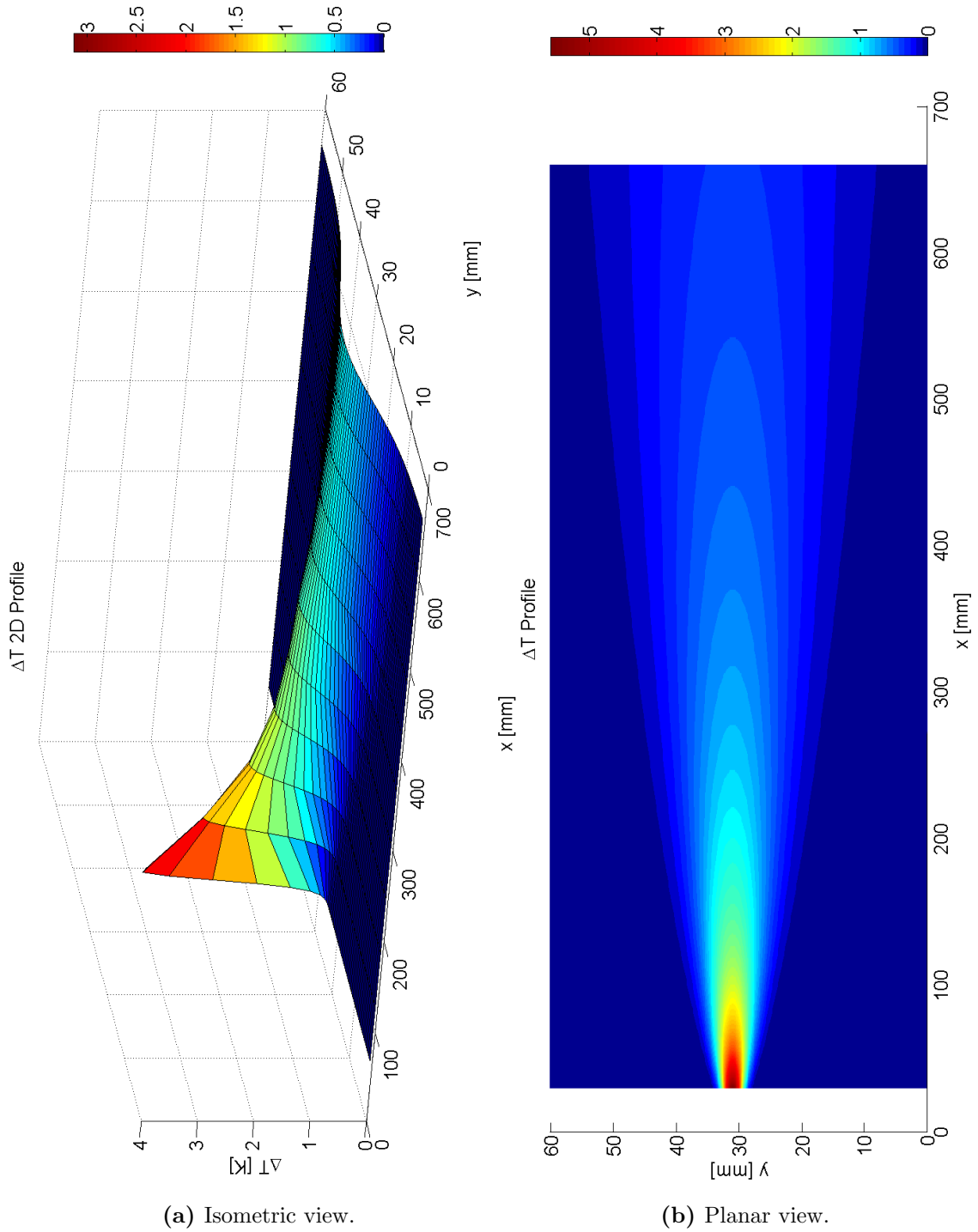


Figure 4.10: Mean temperature excess profile in 2 dimensions. The data is fit to a Gaussian distribution cross-stream, and power-law downstream.

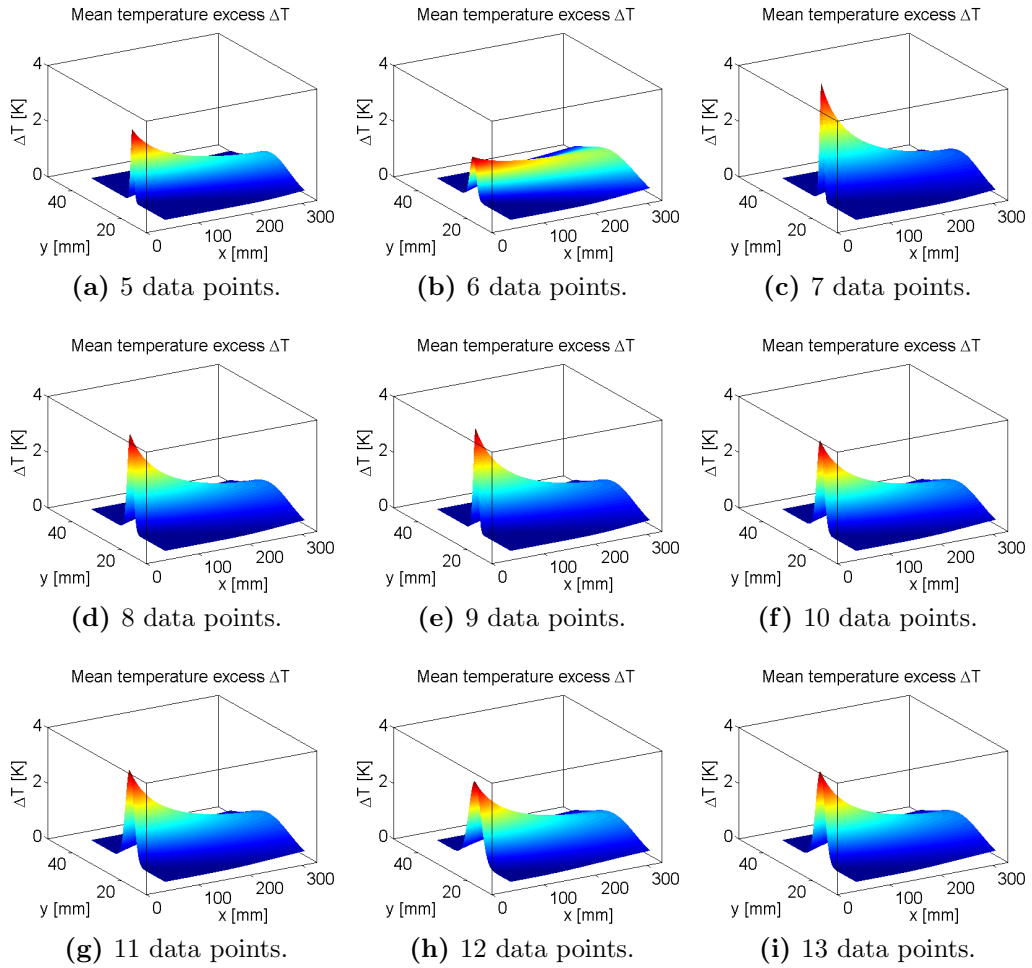


Figure 4.11: Sample search fit evolution, arranged by number of data points taken.

4.4.3 Source Declaration

As a result of time constraints (due to the laboratory being closed for one year during renovations of the Macdonald Engineering Building), a source declaration phase was not fully implemented into the 2D search algorithm. Instead, the model fit was continuously refined until the searcher reached $x/h = 2$. It was observed however that the algorithm was able to make remarkably accurate predictions (particularly for the source location) after very few measurements, and thus an early search termination/source declaration trigger could have been implemented without much loss in accuracy (but a large improvement in search time). With only 6 data points inside the plume, typical predictions of the source location were often ± 1 mm ($0.033h$).

Since the 5-parameter plume model (Equation 4.4) yielded non-physical results ($+\infty$) at the true source location ($x_s = 0$, $y_s/h = 1$), the algorithm instead calculated the properties of the scalar plume at a fixed downstream position of $x/h = 1$. Values for the i) source location (i.e., the profile centre y'_s), ii) parameter's peak value at $x/h = 1$, y'_s (e.g., ΔT_{peak} or $\theta_{rms-peak}$), and iii) profile half-width (i.e., the standard deviation σ_{y_s}) at $x/h = 1$, y'_s were all calculated and logged by the algorithm during each search.

4.4.4 Detailed Results

Results from 30 searches each at five downstream starting positions are shown in Tables 4.3 and 4.4 for the primary search parameters ΔT and θ_{rms} , respectively. All data was recorded at 200 Hz and 10 blocks each of 256 samples per block. The thermal line source power in this case was set to 100 W m^{-1} to improve the signal-to-noise ratio far downstream (particularly for $x/h \geq 10$). Note that ς_p is used to denote the error/width (standard deviation) of the profile of parameter p , which is a convenient

way of denoting the error/scatter in the data. For example, $\varsigma_{\sigma-mean}$ is the width of the profile of all declared values of the standard deviations of the ΔT profile at $x/h = 1$.

As detailed in Tables 4.3 and 4.4, the average y'_s values for all searches were very similar (and slightly offset from $y = 30$ mm, due to an error in positioning the thermal source). As can be seen in the non-dimensionalized declared source location $((y - y'_s)/h)$, the error is typically only $\sim 1\%$. The error in the final predictions is generally lower when the searcher starts farther downstream; this is expected as more data points are used to fit the 2D surface model (since the searcher always continues upstream to $x/h = 1$ as no active source declaration phase was built into the algorithm). Results for the declared value of the search parameter at $x/h = 1$, y'_s are less consistent, but again more accurate when the searcher started farther downstream. Consistent with the 1D search domain results, using the mean temperature excess (ΔT) as a primary search parameter is slightly more accurate for source location than using the rms temperature fluctuation (θ_{rms}). Total search time was dependent primarily on the starting downstream position, since no variation of the number of samples per measurement was studied in these experiments.

A quantitative comparison of the 2D search algorithm results to those that do not incorporate turbulence physics was examined but proved to be difficult owing to the large variation of the experimental/theoretical setup described in the literature. Furthermore, a review of the relevant work (see Chapter 1) showed that most of the existing algorithms are only optimised for specific search conditions. It is suggested that a selection of the algorithms from the literature be implemented in the present experimental apparatus and within the same flow conditions, in order to quantify the real-world benefits of incorporating turbulence physics into source locating algorithms.

Lastly, development of a plume model for the rms-to-mean ratio ($\theta_{rms}/\Delta T$) was briefly attempted in the present work, in keeping with the 1D search results (as well as the literature) that showed this was an optimal primary search parameter. However, it was found the models for ΔT and θ_{rms} could not easily be extended to the peak-to-mean ratio since the ratio does not follow the same Gaussian/power-law form. Unfortunately, due to time constraints imposed by the laboratory closure during renovations, this extension could not be completed, but is instead left as important future work for the project.

Table 4.3: Summary of 2D search results for peak mean temperature difference.

Parameter	Starting x/h				
	5	7	9	11	13
y'_s (mm)	29.63	29.62	29.74	29.69	29.67
$(y - y'_s)/h$	0.012	0.013	0.0087	0.010	0.011
ς_{ys} (mm)	0.538	0.247	0.113	0.100	0.137
ς_{ys}/h	0.018	0.0082	0.0038	0.0033	0.0046
$\Delta T(x/h = 1, y'_s)$ ($^{\circ}\text{C}$)	6.13	6.54	5.98	5.90	5.70
$\varsigma_{\Delta T}$ ($^{\circ}\text{C}$)	6.15	2.58	1.54	1.88	1.87
$\sigma_{mean}(x/h = 1)$ (mm)	3.19	1.28	1.30	1.40	1.39
$\varsigma_{\sigma-mean}$ (mm)	4.14	0.517	0.395	0.718	0.579

Table 4.4: Summary of 2D search results for rms temperature fluctuation.

Parameter	Starting x/h				
	5	7	9	11	13
y'_s (mm)	29.30	29.74	29.63	29.82	29.70
$(y - y'_s)/h$	0.023	0.0087	0.012	0.0060	0.010
ς_{ys} (mm)	0.965	0.773	0.353	0.599	0.246
ς_{ys}/h	0.032	0.026	0.012	0.020	0.0082
$\theta_{rms}(x/h = 1, y'_s)$ ($^{\circ}\text{C}$)	5.31	4.06	4.25	4.42	4.43
$\varsigma_{\theta-rms}$ ($^{\circ}\text{C}$)	4.76	0.922	1.84	1.68	1.13
$\sigma_{rms}(x/h = 1)$ (mm)	2.62	2.02	2.75	2.27	1.89
$\varsigma_{\sigma-rms}$ (mm)	3.63	1.38	2.80	1.60	0.774

Chapter 5

Conclusions and Future Work

5.1 Conclusions

The primary objective of the present work was to develop and test efficient and accurate scalar/contaminant source locating algorithms by attempting to incorporate knowledge of turbulent mixing into the search process. The problem is relevant to two quite distinct problems: i) the ability of animals to detect food or (the scent of) mating partners, and ii) the ability of authorities to locate a release (accidental, terrorist, or other) of a noxious (chemical, biological, or radioactive) substance.

To this end, an easily-configurable one-dimensional search algorithm based on a two-phase hybrid line search with ambient background compensation was developed and tested in a high-aspect-ratio, fully developed turbulent channel flow with a Reynolds number ($Re \equiv \langle U \rangle_{y/h=1} h/\nu$) of 10,800. The scalar under consideration was a small temperature excess emitted from a line source, measured using cold-wire thermometry techniques, and the searcher was a cold-wire probe mounted on a one- (or two-) axis precision traversing mechanism. A detailed description of the experimental apparatus and conditions, as well as a full description of the flow field, was presented.

After performing convergence analysis and determining suitable scalar concentration thresholds, the plume finding (explorative) and plume traversal (exploitive) phases of the search algorithm were designed. The explorative phase used a bio-mimetic ‘zig-zag’ to search the domain until it found the plume. Once the scalar plume was located, the algorithm then moved to the exploitive phase which performed a linear gradient climb to move towards and declare the source location. Multiple primary search parameters were tested including: i) mean temperature excess (ΔT), ii) root-mean-square (rms) temperature fluctuation (θ_{rms}), iii) skewness of the temperature fluctuations (S_θ), iv) kurtosis of the temperature fluctuations K_θ , v) skewness-to-rms ratio (S_θ/θ_{rms}), and vi) rms-to-mean ratio ($\theta_{rms}/\Delta T$). The tradeoff between speed and accuracy was tested for each primary search parameter studied. Overall, the rms-to-mean ratio (a surrogate for peak-to-mean ratio) was found to provide the best combination of speed, accuracy, and robustness to noise in the one-dimensional search case. This was consistent with both the robotics and biology literature in the field. A search for maximum ΔT was found to be slightly quicker than $\theta_{rms}/\Delta T$, but it was significantly more affected by noise.

The benefit of incorporating the physics of turbulent flows is best achieved in a two-dimensional search domain. To this end, the experimental apparatus was modified to give the searcher a planar range of motion. A five-parameter plume model for both the mean scalar concentration (ΔT) and rms fluctuation (θ_{rms}) was created by considering the behaviour of the downstream evolution of the plumes. The model follows a Gaussian profile in the wall-normal direction, and a power-law in the streamwise direction. By combining the plume model with a developed 2D infotactic search algorithm which incorporated the methods of the 1D algorithm and an upwind ‘surge’ component, source location in a 2D search domain was also tested in the present work. Preliminary results indicate that the developed algorithm is both expeditious and accurate, particularly in the case of ΔT as the primary search parameter. Al-

though source declaration was not fully implemented into the 2D algorithm, the results indicated that an appropriate implementation of this feature could reduce the overall search time since the predicted source location was accurate after relatively few (well-placed) measurements by the searcher.

5.2 Future Work

Many possible directions exist for future work on this project. The most immediate task would be to develop a plume model for the rms-to-mean ratio ($\theta_{rms}/\Delta T$), since the results from the 1D search work and the literature showed that this was the optimal search parameter. This was briefly attempted in the present work, but it was found the models for ΔT and θ_{rms} could not easily be extended to the peak-to-mean ratio.

It is also suggested that the relevant algorithm parameters (e.g., zig-zag step size and upstream surge size) be determined with more rigorous theoretical justification. While the chosen values worked well for the present experiments, a theoretical basis for choosing these parameters could help extend the work to other flow conditions. Further work should also be done to refine the source declaration phase, especially of the two-dimensional search algorithms, as this was not examined in much detail in the present work due to time constraints. This could reduce the overall search time of the 2D algorithms based on the preliminary findings of the present work.

In addition, tests and refinement of the algorithms in other types of turbulent flows (e.g., grid turbulence, or the atmospheric boundary layer) would be particularly interesting to determine the universality of the developed algorithms. Large-scale tests in the atmospheric boundary layer would be directly applicable to many industrial scalar source location tasks, such as tracking CBRNE emissions.

More study and independent benchmarking of the existing search algorithms in the literature would also be beneficial in determining the relative performance characteristics of the developed algorithms. This is no small task as the body of literature contains extremely varied flow conditions, methods, and performance characterisations.

A logical next step for the work involves extending the search domain to be three-dimensional (accounting for the fact that in many real-world applications, the searcher will be looking for a scalar/contaminant point source). However, there are certain fundamental impediments to this extension that will require further research (e.g., the fact that many of the baseline search algorithms examined in the present work are not space-filling in a 3D search domain).

Finally, with respect to the computational aspects, simplifying the data processing needs such that time-series data and statistics could be computed and used in real-time would allow for many interesting new search algorithms to be designed and tested, although this would require significant changes to the software and data acquisition equipment.

Bibliography

- BAKER, T. C., FADAMIRO, H. Y. & COSSE, A. A. 1998 Moth uses fine tuning for odour resolution. *Nature* **393** (6685), 530.
- BALKOVSKY, EUGENE & SHRAIMAN, BORIS I. 2002 Olfactory search at high reynolds number. *Proceedings of the National Academy of Sciences of the United States of America* **99** (20), 12589–12593.
- BARBIERI, C., COCCO, S. & MONASSON, R. 2011 On the trajectories and performance of infotaxis, an information-based greedy search algorithm. *Europhysics Letters* **94** (2), 20005.
- BERGER, S A, TALBOT, L & YAO, L S 1983 Flow in curved pipes. *Annual Review of Fluid Mechanics* **15** (1), 461–512.
- BLEVINS, R.D. 1990 *Flow-induced vibration*, 2nd edn. Krieger: Van Nostrand Reinhold.
- BRUUN, H. H. 1995 *Hot-wire anemometry : principles and signal analysis*. Oxford ; New York: Oxford University Press.
- COSTA-PATRY, E. 2005 Mixing of two scalars in turbulent channel flow. Master's thesis, McGill University.
- DIMOTAKIS, P. E. 2005 Turbulent mixing. *Annual Review of Fluid Mechanics* **37**, 329–356.
- HAYES, A. T., MARTINOLI, A. & GOODMAN, R. M. 2002 Distributed odor source localization. *Sensors Journal, IEEE* **2** (3), 260–271.
- LAVERTU, R. A. 2002 Scalar dispersion in turbulent channel flow. Master's thesis, McGill University.
- LAVERTU, R. A. & MYDLARSKI, L. 2005 Scalar mixing from a concentrated source in turbulent channel flow. *Journal of Fluid Mechanics* **528**, 135–172.
- LEMAY, J. & BENAÏSSA, A. 2001 Improvement of cold-wire response for measurement of temperature dissipation. *Experiments in Fluids* **31** (3), 347–356.

- LI, F., MENG, Q. H., BAI, S., LI, J. G. & POPESCU, D. 2008 Probability-pso algorithm for multi-robot based odor source localization in ventilated indoor environments. In *Intelligent Robotics and Applications, Pt I, Proceedings* (ed. C. Xiong, H. Liu, Y. Huang & Y. Xiong), *Lecture Notes in Artificial Intelligence*, vol. 5314, pp. 1206–1215. Berlin: Springer-Verlag Berlin.
- LI, JI-GONG, MENG, QING-HAO, WANG, YANG & ZENG, MING 2011 Odor source localization using a mobile robot in outdoor airflow environments with a particle filter algorithm. *Autonomous Robots* **30** (3), 281–292.
- LI, JI-GONG, MENG, QING-HAO & ZENG, MING 2009 An estimation-based plume tracing method in time-variant airflow-field via mobile robot. In *Robotics and Biomimetics (ROBIO), 2009 IEEE International Conference on*, pp. 2249–2254.
- LI, W., FARRELL, J. A. & CARD, R. T. 2001 Tracking of fluid-advected odor plumes: Strategies inspired by insect orientation to pheromone. *Adaptive Behavior* **9** (3-4), 143–170.
- LO IACONO, G. 2010 A comparison of different searching strategies to locate sources of odor in turbulent flows. *Adaptive Behavior* **18** (2), 155–170.
- LOCHMATTER, T., HEINIGER, N. & MARTINOLI, A. 2009 Localizing an odor source and avoiding obstacles: Experiments in a wind tunnel using real robots. In *Olfaction and Electronic Nose, Proceedings* (ed. M. Pardo & G. Sberveglieri), *AIP Conference Proceedings*, vol. 1137, pp. 69–72. Melville: Amer Inst Physics.
- LOCHMATTER, T. & MARTINOLI, A. 2009 Theoretical analysis of three bio-inspired plume tracking algorithms. In *Robotics and Automation, 2009. ICRA '09. IEEE International Conference on*, pp. 2661–2668.
- LOCHMATTER, THOMAS, RAEMY, XAVIER, MATTHEY, LOIC, INDRA, SAURABH & MARTINOLI, ALCHERIO 2008 A comparison of casting and spiraling algorithms for odor source localization in laminar flow. In *IEEE International Conference on Robotics and Automation, ICRA 2008*, pp. 1138–1143. Pasadena, CA, United states: Institute of Electrical and Electronics Engineers Inc.
- MAFRA-NETO, AGENOR & CARDE, RING T. 1994 Fine-scale structure of pheromone plumes modulates upwind orientation of flying moths. *Nature* **369** (6476), 142–144.
- MARTINEZ, DOMINIQUE 2007 Mathematical physics: On the right scent. *Nature* **445** (7126), 371–372.
- MASSON, J. B., BECHET, M. B. & VERGASSOLA, M. 2009 Chasing information to search in random environments. *Journal of Physics A: Mathematical and Theoretical* **42** (43), 434009.
- MCLEOD, M. 2000 On the design and testing of a high-aspect ratio channel for turbulent flow measurements. *Tech. Rep.*. McGill University.

- MESQUITA, A. R., HESPANHA, J. P. & ASTROM, K. 2008 Optimotaxis: A stochastic multi-agent optimization procedure with point measurements. In *Hybrid Systems: Computation and Control* (ed. M. Egerstedt & B. Mishra), *Lecture Notes in Computer Science*, vol. 4981, pp. 358–371. Berlin: Springer-Verlag Berlin.
- NEVITT, GABRIELLE A., LOSEKOOT, MARCEL & WEIMERSKIRCH, HENRI 2008 Evidence for olfactory search in wandering albatross, *diomedea exulans*. *Proceedings of the National Academy of Sciences* **105** (12), 4576–4581.
- PASTERNAK, Z., BARTUMEUS, F. & GRASSO, F. W. 2009 Levy-taxis: a novel search strategy for finding odor plumes in turbulent flow-dominated environments. *Journal of Physics A: Mathematical and Theoretical* **42** (43), 434010.
- POPE, S. B. 2000 *Turbulent flows*. Cambridge ; New York: Cambridge University Press.
- RUSSEL, R. ANDREW 1999 *Odour detection by mobile robots*. Singapore: World Scientific.
- SETTLES, GARY S. 2006 Fluid mechanics and homeland security. *Annual Review of Fluid Mechanics* **38** (1), 87–110.
- SHRAIMAN, B. I. & SIGGIA, E. D. 2000 Scalar turbulence. *Nature* **405** (6787), 639–646.
- SREENIVASAN, K. R. 1991 On local isotropy of passive scalars in turbulent shear flows. *Proceedings of the Royal Society of London. Series A: Mathematical and Physical Sciences* **434** (1890), 165–182.
- TENNEKES, H. & LUMLEY, JOHN L. 1972 *A first course in turbulence*. Cambridge, Mass.: MIT Press.
- VERGASSOLA, MASSIMO, VILLERMAUX, EMMANUEL & SHRAIMAN, BORIS I. 2007 ‘infotaxis’ as a strategy for searching without gradients. *Nature* **445** (7126), 406–409.
- WARHAFT, Z. 1984 Interference of thermal fields from line sources in grid turbulence. *Journal of Fluid Mechanics* **144**, 363–387.
- WARHAFT, Z. 2000 Passive scalars in turbulent flows. *Annual Review of Fluid Mechanics* **32** (1), 203–240.
- WEBSTER, D.R. & WEISSBURG, M.J. 2009 The hydrodynamics of chemical cues among aquatic organisms. *Annual Review of Fluid Mechanics* **41** (1), 73–90.
- ZARZHITSKY, D., SPEARS, D., THAYER, D. & SPEARS, W. 2004 Agent-based chemical plume tracing using fluid dynamics. In *International Workshop on Formal Approaches to Agent-Based Systems*, , vol. 3228, pp. 146–160. Greenbelt, MD.